Petroleum Science 21 (2024) 3839–3866

Contents lists available at ScienceDirect

Petroleum Science

journal homepage: www.keaipublishing.com/en/journals/petroleum-science

Original Paper

Dynamic evolution mechanism of the fracturing fracture system—Enlightenments from hydraulic fracturing physical experiments and finite element numerical simulation

Qi-Qiang Ren [a, *], Li-Fei Li [a], Jin Wang [b], Rong-Tao Jiang [c], Meng-Ping Li [d, **], Jian-Wei Feng [e]

[a] Institute of Sedimentary Geology, Chengdu University of Technology, Chengdu 610059, Sichuan, China
[b] Sinopec Chongqing Fuling Shale Gas Exploration and Development Company, Chongqing 408000, China
[c] Jianghan Oilfield Oil and Gas Production Capacity Construction Management Center, Chongqing 408000, China
[d] College of Energy, Chengdu University of Technology, Chengdu, 610059, Sichuan, China
[e] School of Resources and Geosciences, China University of Mining and Technology, Xuzhou 221018, Jiangsu, China

ARTICLE INFO

Article history:
Received 25 July 2023
Received in revised form
11 June 2024
Accepted 4 September 2024
Available online 5 September 2024

Edited by Teng Zhu and Min Li

Keywords:
Rock mechanical parameters
Petrophysical experiments
Hydraulic fracturing physical experiment
Finite element numerical simulation
Dynamic evolution mechanism
Fracturing fracture

ABSTRACT

This study aims to elucidate the dynamic evolution mechanism of the fracturing fracture system during the exploration and development of complex oil and gas reservoirs. By integrating methods of rock mechanical testing, logging calculation, and seismic inversion technology, we obtained the current in-situ stress characteristics of a single well and rock mechanical parameters. Simultaneously, significant controlling factors of rock mechanical properties were analyzed. Subsequently, by coupling hydraulic fracturing physical experiments with finite element numerical simulation, three different fracturing models were configured: single-cluster, double-cluster, and triple-cluster perforations. Combined with acoustic emission technology, the fracture initiation mode and evolution characteristics during the loading process were determined. The results indicate the following findings: (1) The extension direction and length of the fracture are significantly controlled by the direction of the maximum horizontal principal stress. (2) Areas with poor cementation and compactness exhibit complex fracture morphology, prone to generating network fractures. (3) The interlayer development of fracturing fractures is controlled by the strata occurrence. (4) Increasing the displacement of fracturing fluid enlarges the fracturing fracture length and height. This research provides theoretical support and effective guidance for hydraulic fracturing design in tight oil and gas reservoirs.

1. Introduction

Constrained by the low porosity and permeability inherent in unconventional oil and gas resources, particularly in shale/tight oil and gas formations, effective hydraulic fracturing played an increasingly pivotal role in enhancing production and exploitation by augmenting permeability (Zoback, 2019; Chen et al., 2021; Zhao et al., 2022a). Influenced by fluid injection, high pressure was generated around wells, creating new fracture networks or activating natural fractures to maximize production from shale/tight oil and gas reservoirs (Freeman et al., 2011; Vermylen and Zoback, 2011; Tan et al., 2022). However, due to variations in stress and fracture propagation, several shale/tight oil and gas wells exhibit low productivity post-fracturing (Wei et al., 2021; Luo et al., 2021; Ren et al., 2022). To achieve effective hydraulic fracturing in shale/tight oil and gas reservoirs, a detailed analysis of rock mechanical properties (including anisotropic characteristics), current in-situ stress distribution, and natural fracture characteristics is imperative (Wu et al., 2014; Lin et al., 2017; Morley et al., 2017, 2018; Zhao et al., 2022a). The artificial fracture network can furnish additional channels for oil and gas migration and storage from pores and natural fractures, thereby enhancing production capacity (Pope et al., 2012; Bhattacharya and Nikolaou, 2016; Zhang et al., 2021; Tan et al., 2022). During the hydraulic fracturing process, physical and chemical interactions occur, altering rock mechanical

* Corresponding author.
** Corresponding author.
E-mail addresses: renqq2017@163.com (Q.-Q. Ren), 1159064919@qq.com (M.-P. Li).

https://doi.org/10.1016/j.petsci.2024.09.004

properties such as Young's modulus, Poisson's ratio, and porosity (Dehghanpour et al., 2012; Westwood et al., 2017; Lyu et al., 2019; Fatah et al., 2021). Consequently, influenced by in-situ stress variations and natural fractures, the initiation and expansion patterns of hydraulic fractures exhibit distinct features (Chang et al., 2018, 2022; Hou et al., 2019; Diaz et al., 2020).

Two significant numerical simulation methods have been distinguished for studying the propagation behavior of fracturing fractures: discrete fracture modeling and finite element modeling (Miehe et al., 2015; Lu et al., 2015; Zeng et al., 2018; Ren et al., 2019; Zhu et al., 2021; Huang et al., 2022, 2023). Essentially, the finite element method can be applied to analyze the strongly heterogeneous rock and the propagation of multiple fractures during hydraulic fracturing (Li et al., 2016; Rege and Lemu, 2017; Ren et al., 2020; Zhao et al., 2022b). However, the finite element method primarily captures short-term mechanical behavior during the loading process, and the simulation of continuous mechanical processes remained a challenge (Rabczuk et al., 2010; Wick, 2016; Ren et al., 2021; Yang and Gao, 2022). Numerous studies have investigated the effects of interlayers, pre-fractures, and rock heterogeneity on fracture initiation and propagation during hydraulic fracturing, employing laboratory investigations and numerical simulation (Wang et al., 2015; Aimene et al., 2019; Ju et al., 2019; Zhou et al., 2020; Zheng et al., 2022). Understanding the genetic mechanisms of natural fractures (shear and tensile fractures) can support the evolution of rock permeability and fracture prediction in shale/tight formations (Lorenz and Hill, 1994; Laubach and Diaz-Tushman, 2009; Hooker et al., 2017; Su et al., 2022). Several scholars have employed multi-scale characterization methods, including core observation, outcrop investigation, thin section analysis, scanning electron microscope experiments, computer tomography, logging identification, and seismic interpretation, to study natural fractures (Renshaw and Pollard, 1995; Laubach and Diaz-Tushman, 2009; Hooker et al., 2017; Zhang et al., 2022a; Yu et al., 2022). Consequently, the obtained outcomes can be applied to conduct research on hydraulic fracturing regarding fracture activation and propagation (Zou et al., 2017; Ranjith et al., 2018; Hu et al., 2022).

Additionally, a series of petrophysical experiments were conducted, encompassing uniaxial and triaxial rock mechanical experiments, acoustic emission testing, and anisotropy testing, aimed at comprehending the stress-strain curve, fracturing initiation, propagation, and evolution process during hydraulic fracturing (Laubach, 2003; Gale et al., 2014; Tan et al., 2022; Nguyen-Le and Shin, 2022). Stumpf et al. (2009) investigated the dynamic evolution of fracture development in ductile rocks and analyzed configurational forces. Zhao et al. (2022c) addressed the unique characteristics of shale gas, employing X-ray computed tomography and acoustic emission to analyze the effects of hydrostatic pressure on hydraulic fracturing properties. Through experimental investigation, studies explored proppant settling, brittleness, fracture initiation, and hydraulic fracture propagation in various lithologies during the hydraulic fracturing process (Bostrom et al., 2014; Wen et al., 2016; Chen et al., 2021; He et al., 2022; Zhao et al., 2022a). Analyzing the mechanical properties and fracture evolution characteristics of roadway sandstone constrained by various angles of weakly filled joints, researchers conducted rock mechanical testing (Mathews et al., 2017; Niu et al., 2021; Su et al., 2022; Zhou et al., 2022). Furthermore, non-monotonic fracture evolution, dynamic phase-field fracture, dynamic mechanical responses, and damage evolution during various fracturing were systematically researched through different experimental investigations (Li et al., 2022; Weinberg and Wieners, 2022; Zhang et al., 2022b; Chen et al., 2022). Notably, studies summarized vertical fracture propagation, diverted fracture geometry, flow conductivity characteristics, and fracture generation during various injection methods and different temporary plugging fracturing using computed tomography and triaxial mechanical experiments (Williams et al., 2016; Kim et al., 2018; Li et al., 2022; Cao et al., 2022; Chang et al., 2022). However, there is limited research on the dynamic evolution mechanism of the fracturing fracture system under different cluster perforations in various lithological combinations. It is imperative to conduct such studies by coupling hydraulic fracturing physical experiments with finite element numerical simulation based on refined rock mechanical characterization.

In this manuscript, we aim to elucidate the dynamic evolution mechanism of the fracturing fracture system during the exploration and development of complex tight oil and gas reservoirs. Rock mechanical testing, logging calculation, and seismic inversion technology were employed to obtain the current in-situ stress characteristics of a single well and rock mechanical parameters, such as Young's Modulus and Poisson's Ratio. Additionally, through rock mechanical testing, including triaxial mechanical testing and acoustic emission testing, the significant controlling factors of rock mechanical properties were analyzed. Drawing reference from typical lithological combinations, we configured three different fracturing models: single-cluster perforation, double-cluster perforation, and triple-cluster perforation. Subsequently, by coupling hydraulic fracturing physical experiments with finite element numerical simulation and integrating acoustic emission technology, the fracture initiation mode and evolution characteristics during the loading process were determined. This study can offer theoretical support and effective guidance for hydraulic fracturing design in tight oil and gas reservoirs.

2. Geological setting

The Songliao Basin, situated in the northeast of China, spans approximately 820 km in length from north to south and 350 km in width from east to west, trending in a northeast direction (Feng et al., 2010; Wang et al., 2016). Surrounded by mountains, the basin covers a total area of 260,000 km^2, making it the largest Mesozoic-Cenozoic petroliferous basin in China (Wu et al., 2001; Feng et al., 2012; Wang et al., 2016). The Songliao Basin comprises six sub-structures: the southwest uplift, the western slopes, the northern subsidence, the northeast uplift, the southeast uplift, and the central depression (Fig. 1a). Further subdivision reveals the central depression composed of six distinct sub-structures: the Taikang uplift, the Longhupao-Daan terrace, the Qijia-Gulong sag, the Daqing placanticline, the Sanzhao sag, and the Mingshui terrace (Fig. 1b) (Lin et al., 2003; Huang et al., 2019). The Xinzhao oil field lies to the south of the Daqing placanticline, while the Zhoufu oil field is situated southeast of the Sanzhao sag (Wang et al., 2016; Xia, 2020). Three significant tectonic evolution stages have been identified in the area: the faulting depression stage, the depression stage, and the shrinking stage, each characterized by distinct boundary conditions, sedimentation mechanisms, and kinetic backgrounds (Chen et al., 1999). Illustratively, the Xinzhao oil field exhibits a complex fault system (Fig. 1c), whereas the Zhoufu oil field is characterized by several major faults (Fig. 1d), showcasing two different structural characteristics in the study area (Huang et al., 2019; Xia, 2020). The study area predominantly features Cretaceous continental sedimentary formations with a total thickness exceeding 7000 m, indicating the most complete continental Cretaceous sedimentary strata globally (Feng et al., 2010). Four key oil and gas formations have been identified in the study area: the Nenjiang Formation, the Yaojia Formation, the Qinshankou Formation, and the Quantou Formation (W. Chen et al., 2010; Huang et al., 2019). Furthermore, six significant reservoirs have been

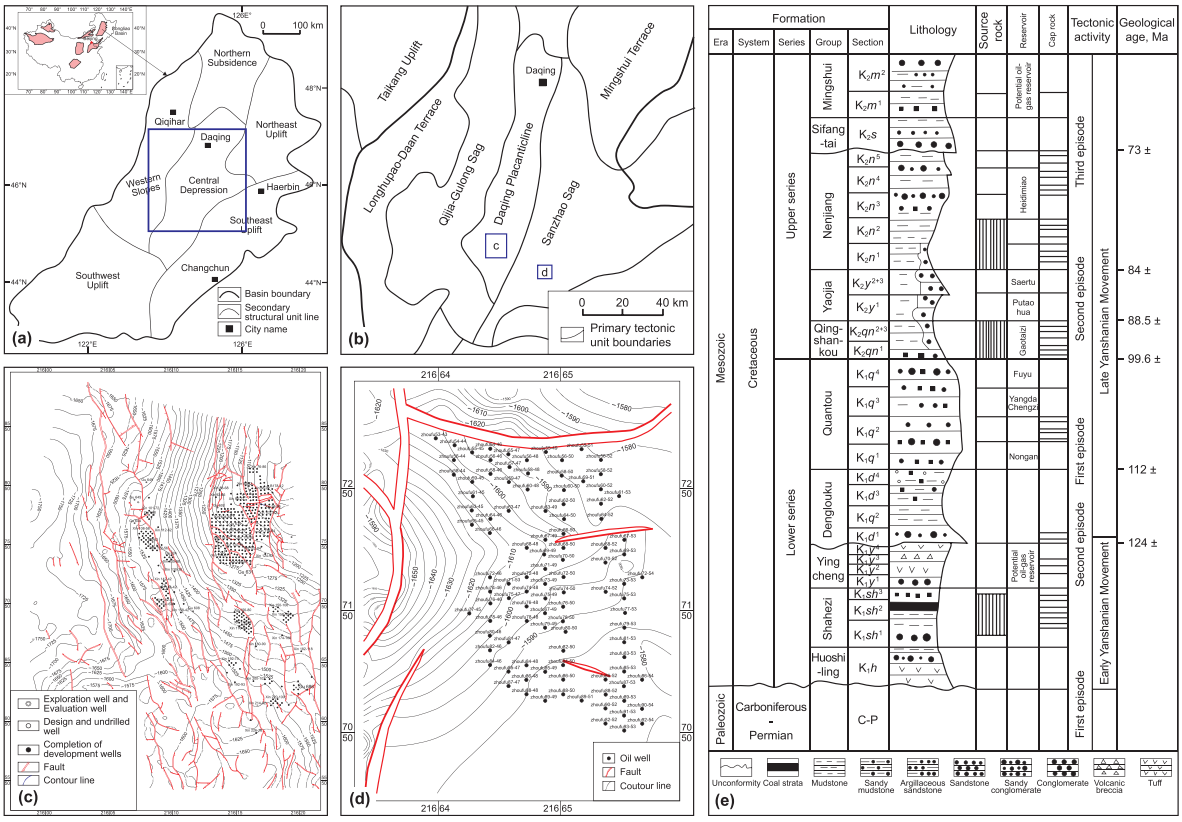

Fig. 1. The regional location and structural characteristics of study area. **(a)** is the structural characteristics of Songliao basin; **(b)** refers to the geographical location of Daqing placanticline and Sanzhao sag; **(c)** shows the structure map of Xinzhao area; **(d)** is the structure map of Zhoufu area; **(e)** refers to the stratigraphic features in the Mesozoic formation in the study area.

distinguished: the Saertu, Putaohua, Gaotaizi, Fuyu, Yangdachengzi, and Nongan reservoirs (Si et al., 2021). The Putaohua reservoir, located in the middle-lower part of the first section of the Yaojia Formation, boasts a thickness of 40–60 m (Fig. 1e). Its lithology comprises gray and gray-green mudstone, with transitional lithology interspersed with gray and dark gray siltstone (Wang et al., 2016; Huang et al., 2019).

Constrained by the lithologic assemblage, cyclicity, and vertical development degree of sandstone in the Putaohua reservoir, three sand Formations and eleven sublayers were distinguished (Fu and Song, 2008; Si et al., 2021). The debris of feldspar sandstone in the target strata (Putaohua oil reservoir) consisted of fine particles, generally in the silt grade, with poorly developed pores (Xia, 2020). Three main cementation types were identified: film, filling film, and filling-regeneration cementation. The Putaohua oil reservoir was characterized by primary intergranular pores, with a mass fraction of argillaceous material at 10.30% (X. Chen et al., 2010). Moreover, the Putaohua oil layer in the study area represented a medium-low porosity and low to ultra-low permeability reservoir. Porosity mainly ranged from 10% to 20%, with an average of 12.40%. Permeability was primarily distributed between 0.30×10^{-3} and 99.20×10^{-3} μm^2, with an average of 2.77×10^{-3} μm^2 (Sun et al., 2018; Xia, 2020). Through core observation and outcrop statistics, two significant types of fractures were distinguished: structural fractures and nonstructural fractures (Zeng et al., 2022; Fu et al., 2023; Gong et al., 2023). The greater the extension of the fracture or the depth of the longitudinal cut, the wider the fracture aperture and spacing became (Huang et al., 2019). The fracture density exhibited a low development degree, with an average value of 0.03 fractures/m. Due to the low fracture density, natural fractures played only a secondary role in forming fracturing fracture networks in tight sandstone reservoirs. Constrained by the underdevelopment of natural fractures in the tight sandstone, the relationship between shear stress and fracturing fracture was examined. Rock mechanical testing was conducted to analyze mechanical parameters under different stress conditions. When shear stress exceeded rock shear strength, induced fractures were more easily generated. The dynamic evolution mechanism of the fracturing fracture system under various cluster hole methods and lithologic assemblages remains unclear.

3. Testing and technology

3.1. Sampling and rock mechanical testing

Thirty specimens of various lithologies (Quantou Formation and Yaojia Formation) from different wells were selected for rock mechanical testing at Qingdao Jiahang Petroleum Technology Corporation in Shandong University of Science and Technology (Table 1). A TAW-100 triaxial stress testing machine was utilized for the rock mechanical testing. The testing force measurement accuracy was set at 1.00%, with a temperature of 180 °C. Three key mechanical parameters of different specimens were obtained under normal pressure and temperature: Young's modulus, Poisson's ratio, and compressive strength. Additionally, three significant confining pressures were applied during the triaxial mechanical testing: 15.00 MPa, 25.00 MPa, and 35.00 MPa. The cohesion and internal friction angle in different lithologies were then determined (Table 2). Strategically, to analyze the influence of different water-oil ratios on rock mechanical parameters, the rock samples were

Table 1
The sampling information and numbers in the rock mechanical testing in the study area.

Location	Well	Formation	Lithology	Depth, m	Number
Zhoufu area	Zhoufu59-51	K_1q^4	Argillaceous siltstone	1834.35	1
	Zhoufu59-51	K_1q^4	Argillaceous sandstone	1836.67	2
	Zhoufu59-51	K_1q^4	Fine sandstone	1836.90	3
	Zhoufu59-51	K_1q^4	Fine-medium sandstone	1838.00	4
	Zhoufu59-51	K_1q^4	Fine-medium sandstone	1838.93	5
	Zhoufu59-51	K_1q^4	Gravelly medium sandstone	1839.95	6
Xinzhao area	Xin124-75	K_2y^1	Argillaceous siltstone	1420.80	7
	Xin124-69	K_2y^1	Siltstone	1396.40	8
	Xin124-69	K_2y^1	Medium sandstone	1397.40	9
	Xin124-69	K_2y^1	Medium sandstone	1397.75	10
	Xin124-69	K_2y^1	Argillaceous siltstone	1398.20	11
	Xin124-69	K_2y^1	Fine sandstone	1425.31	12
	Xin124-69	K_2y^1	Fine-medium sandstone	1399.00	13

Table 2
The testing results of triaxial mechanical testing in different lithologies.

Location	Testing number	Lithology	CP, MPa	Strength, MPa	*E*, GPa	μ	Co-, MPa	IFA, °
Zhoufu area	2-1	Argillaceous sandstone	25.00	153.83	19.957	0.236	30.28	29.79
	2-2		35.00	173.58	16.336	0.240		
	6-1	Gravelly medium sandstone	15.00	122.37	25.687	0.354	23.57	32.74
	6-2		25.00	143.86	14.645	0.225		
	6-3		35.00	169.47	16.925	0.187		
Xinzhao area	9-1	Medium sandstone	35.00	85.54	12.842	0.226	22.14	16.38
	9-2		25.00	81.04	8.461	0.168		
	9-3		15.00	69.83	6.735	0.167		
	11-1	Fine sandstone	25.00	139.58	18.856	0.117	33.71	24.35
	11-2		35.00	153.61	19.206	0.286		

Where the CP is confining pressure, MPa; *E* is the Young's modulus, GPa; μ refers to the Poisson's ratio; Co- is the cohesion, MPa; IFA shows the internal friction angle, °.

soaked in water for 30 min (Table 3). Subsequently, the uniaxial stress testing machine was employed to assess the variation of mechanical properties in rocks with various water-oil ratios.

3.2. Well logging data calculation (in-situ stress and mechanical parameters)

The well logging data and stress calculation model provided an effective and rapid means of obtaining current in-situ stress, with accuracy reaching up to 95% (Wang et al., 2014). Ten typical wells were selected to conduct well logging calculations of reservoir rock mechanical parameters. Using shear-wave and portrait-wave data, Young's modulus and Poisson's ratio were calculated based on Eqs. (1) and (2). Incorporating rock mechanical theory and research findings on reservoir characteristics, Young's modulus and Poisson's ratio from mechanical testing were used to modify and validate the calculation model. An integrated calculation and interpretation process were then outlined, where rock mechanical testing provided discrete point-like mechanical parameters, and well logging data calculation was used to determine continuous mechanical parameters in single wells. Based on the obtained rock mechanical parameters, an optimized computational model was selected to calculate the in-situ stress of each well. Horizontal maximum principal stress was computed using Poisson's ratio and rock pore pressure, as per Eq. (3), while the horizontal minimum principal stress was derived from Eq. (4). Considering rock density and depth, vertical principal stress was calculated using Eq. (5). Consequently, distribution characteristics of Young's modulus, Poisson's ratio, horizontal maximum principal stress, horizontal minimum principal stress, and vertical principal stress were obtained. Notably, various rock mechanical parameters and in-situ stress values in different lithologies were also determined. Simultaneously, the method of image logs was employed to determine the current stress field direction through the study of induced fractures.

$$E = \frac{\rho\left(3\Delta t_s^2 - 4\Delta t_p^2\right)}{\Delta t_s^2\left(\Delta t_s^2 - \Delta t_p^2\right)} \times 10^4 \tag{1}$$

Table 3
The testing information of moisture content in oil-water mixture liquor in different rock samples in the study area.

Location	Testing number	Lithology	Soaking time, minutes	Moisture content, %
Xinzhao area	7-1A	Argillaceous siltstone	30	60
	7-1B			100
	7-2A			0
	7-2B			40
Zhoufu area	4-2A	Fine-medium sandstone	30	100
	4-2B			0
	4-3A			60
	4-3B			40

$$\mu = \frac{0.5\Delta t_s^2 - \Delta t_p^2}{\Delta t_s^2 - \Delta t_p^2} \tag{2}$$

Where E is Young's modulus, MPa; μ refers to the Poisson's ratio, dimensionless; ρ shows the rock density, kg/m^3; Δt_s and Δt_p refer to the time difference of shear wave and portrait-wave, respectively, μs/ft.

$$S_H = \frac{1}{2}\left[\frac{\xi_2 E}{1-\mu} + \frac{2\mu}{1-\mu}(S_V - \alpha P_P) + \frac{\xi_2 E}{1+\mu}\right] + \alpha P_P \tag{3}$$

$$S_h = \frac{1}{2}\left[\frac{\xi_1 E}{1-\mu} + \frac{2\mu}{1-\mu}(S_V - \alpha P_P) + \frac{\xi_1 E}{1+\mu}\right] + \alpha P_P \tag{4}$$

$$S_V = \int_0^H \rho_{(h)} g dh \tag{5}$$

where S_H is the horizontal maximum principal stress, MPa; S_h is the horizontal minimum principal stress, MPa; S_V is the vertical principal stress, MPa; ξ_1 and ξ_2 show the horizontal tectonic stress coefficient, dimensionless; α is the Boit coefficient, dimensionless; E is the rock Young's modulus, MPa; μ refers to the rock Poisson's ratio, dimensionless; P_p is the pore pressure, MPa; H refers to the depth, m; $\rho_{(h)}$ is the density of the overlying strata (a function related to the depth h), g/cm^3; g refers to the gravitational acceleration, m/s^2. During the calculation model, the horizontal tectonic stress coefficient and the Boit coefficient were obtained by the correction and reverse calculation with the measured results of in-situ stress.

3.3. Hydraulic fracturing physical simulation experiment

A TAW-100 triaxial stress testing machine was utilized to apply the triaxial confining stress. The physical simulation experiment comprised four key processes: model sample preparation, experiment preparation, experiment execution, and photo observation (Fig. 2). During model sample preparation, three significant vertical rock lithological combinations were configured from top to bottom: mudstone with siltstone-argillaceous siltstone-silty mudstone (Fig. 3a), silty mudstone-siltstone-mudstone (Fig. 3b), and mudstone-sandstone-mudstone (Fig. 3c). Additionally, a lithological combination of silty mudstone-siltstone-mudstone was configured from left to right to simulate the fracturing fracture in the siltstone, representing the horizontal fracturing period (Fig. 3d). Three different cluster perforation types were employed to simulate hydraulic fracturing in typical wells: single cluster perforation, double cluster perforation, and triple cluster perforation. In Model I, comprising the single cluster perforation, double cluster perforation, and triple cluster perforation, fracturing fracture characteristics were studied under loading stresses of 41.5, 31, and 37.4 MPa (Fig. 3a). Model II involved the double cluster perforation and triple cluster perforation to analyze fracturing fracture under stress conditions of 39, 28, and 34.3 MPa (Fig. 3b). Model III featured the single cluster perforation and double cluster perforation under loading stresses of 39.00, 28.00, and 34.30 MPa (Fig. 3c). In Type IV, the double cluster perforation was applied to analyze fracturing fracture in horizontal wells and observe the distribution characteristics of fracturing fractures (Fig. 3d). Simultaneously, the ZH7137 acoustic emission (AE) equipment was used to record the dynamic evolution process of fracturing fractures in real-time. The hydraulic fracturing physical simulation experiment and AE experiment were conducted at Qingdao Jiahang Petroleum Technology Corporation in Shandong University of Science and Technology.

Referencing the obtained mechanical parameters, similar lithology, thickness, rock mechanical parameters, rock cementation, permeability, displacement, and confining pressure were configured to replicate the real evolutionary process of fracturing fractures. In Model I, the following parameters were set: Young's modulus, Poisson's ratio, density, and thickness were 2.20 GPa, 0.33, 2.20 g/cm^3, and 30.00 mm, respectively, for mudstone with siltstone; 2.70 GPa, 0.25, 2.40 g/cm^3, and 20 mm, respectively, for argillaceous siltstone; and 2.20 GPa, 0.35, 2.00 g/cm^3, and 30 mm, respectively, for silty mudstone (Table 4). In Model II, the parameters were as follows: Young's modulus, Poisson's ratio, density, thickness, permeability, and porosity were set to 2.70 GPa, 0.24, 2.04 g/cm^3, 40.00 mm, 0.51 mD, and 16.41%, respectively, for silty mudstone; 3.00 GPa, 0.17, 1.89 g/cm^3, 20.00 mm, 10.205 mD, and 26.82%, respectively, for siltstone; and 1.70 GPa, 0.35, 2.17 g/cm^3, 40.00 mm, 0.27 mD, and 9.42%, respectively, for mudstone. For Model III, the parameters were set as follows: Young's modulus, Poisson's ratio, density, thickness, permeability, and porosity were 1.70 GPa, 0.22, 2.17 g/cm^3, 40.00 mm, 0.27 mD, and 9.42%, respectively, for mudstone; and 3.00 GPa, 0.17, 2.00 g/cm^3, 20.00 mm, 10.20 mD, and 20.82%, respectively, for sandstone. Additionally, in Model IV, the parameters were set as follows: Young's modulus, Poisson's ratio, density, and thickness were 2.40 GPa, 0.30, 2.20 g/cm^3, and 30.00 mm, respectively, for silty mudstone; 2.80 GPa, 0.22, 2.60 g/cm^3, and 40.00 mm, respectively, for siltstone; and 2.00 GPa, 0.35, 2.00 g/cm^3, and 30.00 mm, respectively, for mudstone.

3.4. Finite element numerical simulation

A three-dimensional (3-D) geomechanical model was established using finite element numerical simulation (FENS). In FENS, the continuous geological body was discretized into numerous finite elements, and then numerical solutions were obtained (Hunt et al., 2011; Liu et al., 2017; Ren et al., 2019; Andhumoudine et al., 2021). Displacement, stress, and strain were the three fundamental variables in FENS. Utilizing interpolation functions, the displacement of each node was determined, leading to the calculation of internal stress and strain. Consequently, the tectonic stress field was computed by integrating these discretized units across the entire geological body. The simulation accuracy was notably influenced by the fidelity to the actual geological model, including the number of nodes and elements (Islam et al., 2009; Mohammadnejad and Andrade, 2016). Four primary operation steps in FENS were identified: establishing the geological model (Step I), generating the finite element mesh (Step II), setting up the mechanical model (Step III), and defining the boundary loading conditions (Step IV).

During Step I, the model size and lithological combinations were determined based on the model types utilized in the hydraulic fracturing physical experiment. In Step II, the continuous geological model was partitioned into numerous elements interconnected by nodes. Rock mechanical parameters, such as Young's modulus and Poisson's ratio, obtained from logging data calculations and rock mechanical testing, were assigned to the discretized elements during Step III. In Step IV, guided by the loading methods employed in the hydraulic fracturing physical experiment, boundary load conditions including force and displacement were set at the corresponding boundaries. Three different models were established to investigate stress variation and fracture characteristics during the fracturing process (Fig. 4). Vertical lithological combinations of mudstone with siltstone-argillaceous siltstone-silty mudstone (Fig. 4a), horizontal lithological combinations of silty mudstone-siltstone-mudstone (Fig. 4b), and argillaceous siltstone (Fig. 4c) were configured for the FENS. The depth of the single-cluster

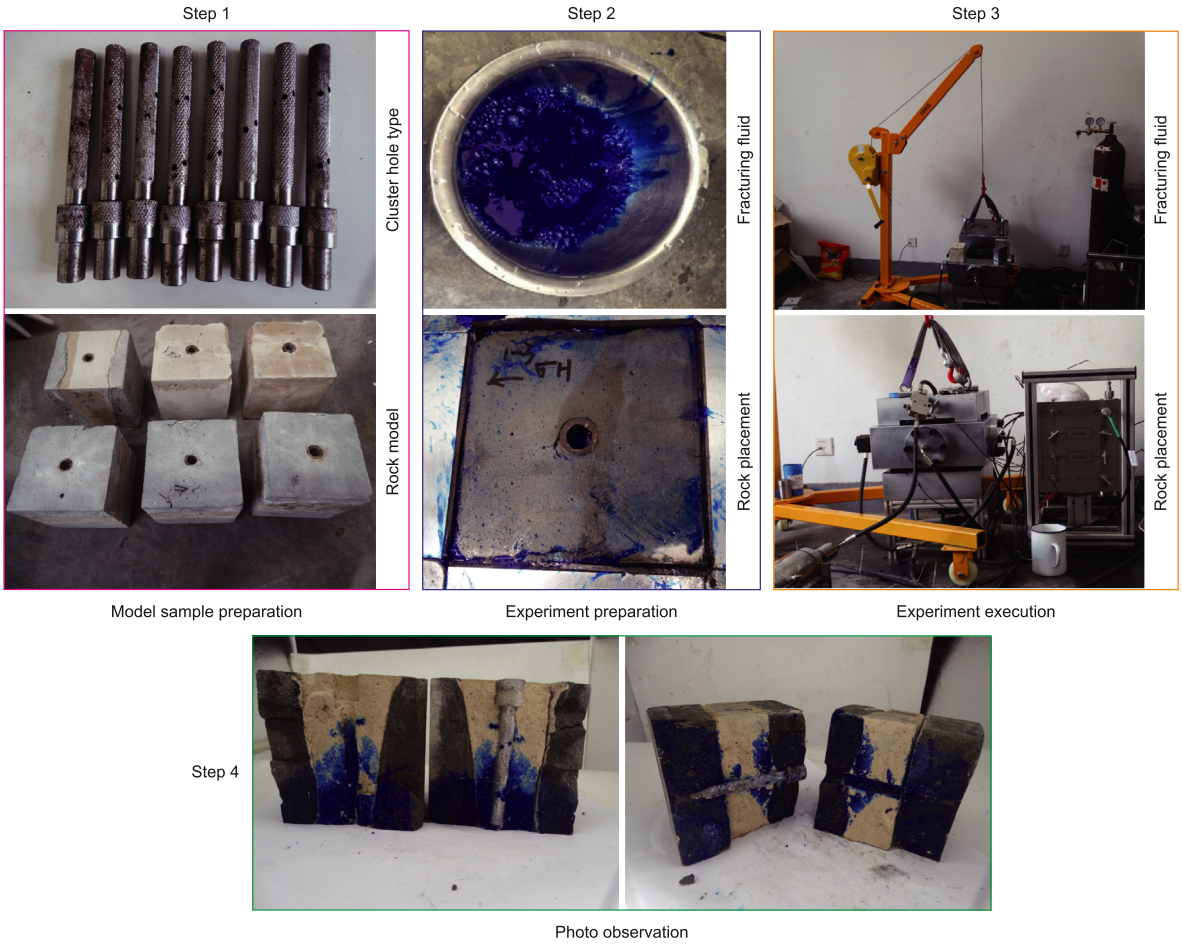

Fig. 2. The experimental configuration and procedure of hydraulic fracturing physical simulation experiment.

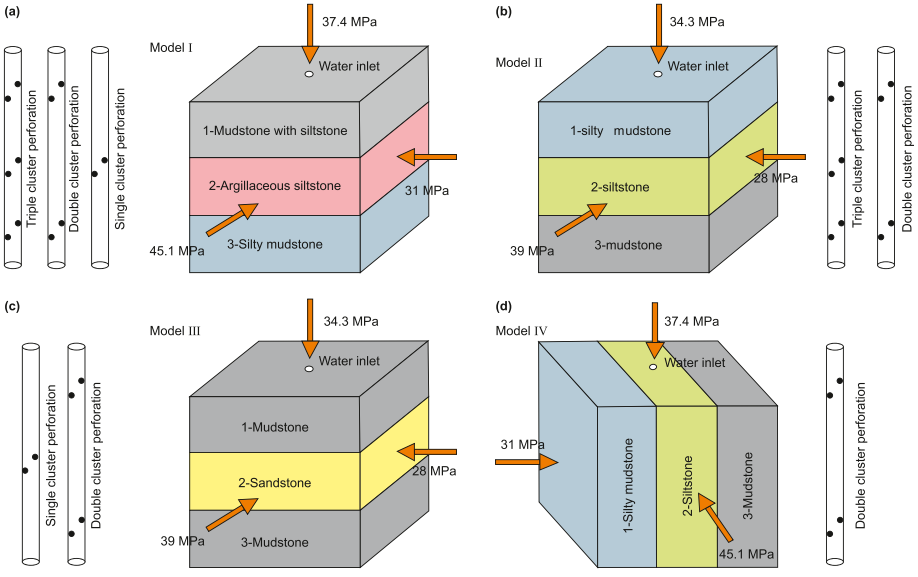

Fig. 3. The lithological combination and cluster perforation type during the hydraulic fracturing physical experiment. **(a)** is stress loading type and lithological combination of mudstone with siltstone-argillaceous siltstone-silty mudstone, indicating three different cluster perforation methods; **(b)** refers to the lithological combination of silty mudstone-siltstone-mudstone, performing two different cluster perforation methods; **(c)** shows to the lithological combination of mudstone-sandstone-mudstone, indicating two different cluster perforation methods; **(d)** refers to the lithological combination of silty mudstone-siltstone-mudstone horizontally, performing double cluster perforation methods.

Table 4
The configured mechanical parameters in different models in the hydraulic fracturing physical experiment.

Group	Layer	Lithology	E, GPa	μ	ρ, g/cm^3	Thickness, mm	Permeability, mD	Porosity, %
I	1	Mudstone with siltstone	2.20	0.33	2.2	30	/	/
	2	Argillaceous siltstone	2.70	0.25	2.4	40	/	/
	3	Silty mudstone	2.00	0.35	2.0	30	/	/
II	1	Silty mudstone	2.70	0.24	2.06	40	0.51	16.41
	2	Siltstone	3.00	0.17	1.89	20	10.205	26.82
	3	Mudstone	1.70	0.35	2.17	40	0.27	9.42
III	1	Mudstone	1.70	0.22	2.17	40	0.27	9.42
	2	Sandstone	3.00	0.17	2.0	20	10.2	26.82
	3	Mudstone	1.70	0.22	2.17	40	0.27	9.42
IV	1	Silty mudstone	2.40	0.30	2.2	30	/	/
	2	Siltstone	2.80	0.22	2.6	40	/	/
	3	mudstone	2.00	0.35	2.0	30	/	/

where E is the Young's modulus, GPa; μ refers to the Poisson's ratio.

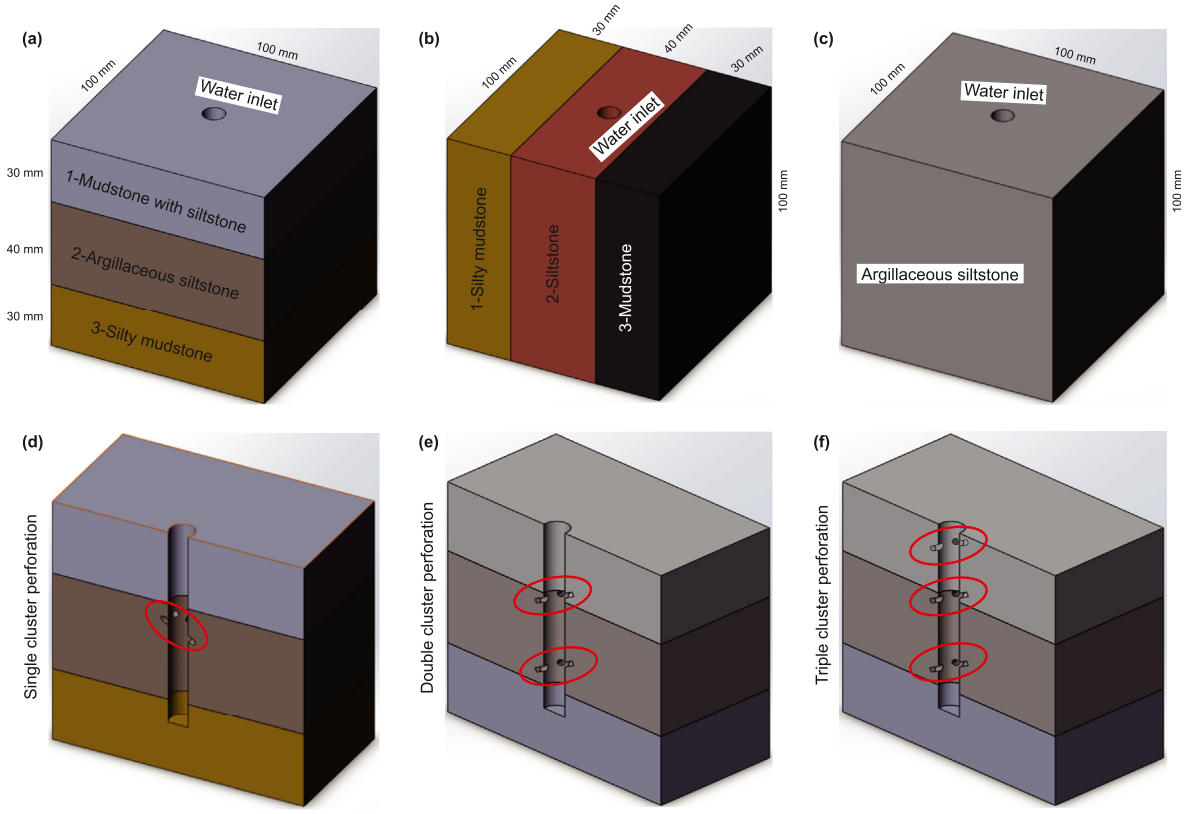

Fig. 4. The lithological combination and cluster perforation type during the finite element numerical simulation. **(a)** is lithological combination of mudstone with siltstone-argillaceous siltstone-silty mudstone; **(b)** refers to the lithological combination of silty mudstone-siltstone-mudstone; **(c)** shows to the lithological combination of argillaceous siltstone; **(d)** refers to the simple cluster perforation; E is the double cluster perforation; e refers to the triple cluster perforation.

perforation was 80 mm, with an aperture of 10 mm (Fig. 4d). The double-cluster perforation had a depth of 80 mm and an aperture of 10 mm, with the upper shoot cluster hole positioned 30 mm from the top and the lower shoot cluster hole positioned 60 mm from the top (Fig. 4e). The rock mechanical parameters used in the FENS were referenced from the mechanical parameters obtained in the hydraulic fracturing physical experiment and are listed in Table 5.

Table 5
The rock mechanical parameters in different lithologies in the finite element numerical simulation.

Lithology	Young's modulus, GPa	Poisson's ratio	Density, kg/m^3
Mudstone with siltstone	27	0.20	2400
Argillaceous siltstone	25	0.25	2000
Silty mudstone	21	0.33	1600
Mudstone	20	0.35	1400
Siltstone	28	0.20	2400

4. Results

4.1. Mechanical parameters of rock mechanical testing

Based on the results of uniaxial and triaxial mechanical testing (Table 2, Fig. 5a, b, c, and d), significant differences were observed in the rock mechanical properties, indicating strong heterogeneity and rapid lithology phase transition. As the stress loading progressed, the rock ruptured suddenly at point A, followed by continuous rupture and displacement enlargement at point B. According to the rock mechanical testing results (Table 2, Fig. 5e, f, g, and h), the Young's modulus and Poisson's ratio of argillaceous sandstone in the Zhoufu area ranged from 16.34 to 19.96 GPa and 0.23 to 0.24, respectively. The cohesion and internal friction angle of argillaceous sandstone were determined to be 30.28 MPa and 29.79°, respectively. The Young's modulus and Poisson's ratio of gravelly medium sandstone ranged from 14.65 to 25.69 GPa and 0.19 to 0.35, with a cohesion of 23.57 MPa and an internal friction angle of 32.74°. Additionally, the Young's modulus and Poisson's ratio of medium sandstone in the Xinzhao area were found to be 6.74–12.84 GPa and 0.17 to 0.23, respectively, with a cohesion of 22.14 MPa and an internal friction angle of 16.38°. The Young's modulus and Poisson's ratio of fine sandstone ranged from 18.86 to 19.21 GPa and 0.12 to 0.29, with a cohesion of 33.71 MPa and an internal friction angle of 24.35°. An increase in argillaceous content led to decreased rock strength and Young's modulus. Coarser grain size resulted in larger rock cohesion, and smaller internal friction angle and coefficient compared to fine-grained rock (Fig. 5e, f, g, and h).

As the moisture content in the oil-water mixture increased, the Young's modulus initially decreased (water content: 0%–60%, oil content: 100%–40%), followed by a gradual increase (water content: 60%–100%, oil content: 40%–0%) (Fig. 6a). Poisson's ratio exhibited a positive correlation with moisture content in the oil-water mixture (Fig. 6b), mainly ranging between 0.15 and 0.35, and rarely exceeding 0.40. For example, in specimens No.7 (argillaceous sandstone) and No.4 (fine-medium sandstone), the uniaxial compressive strength initially decreased, then increased with rising water-oil ratios (Fig. 6c and d). In argillaceous sandstone, the Young's modulus values were 15.60, 11.30, 9.60, and 10.10 GPa for rock with 0%, 40%, 60%, and 100% moisture content in the oil-water mixture, respectively (Fig. 6a). The Poisson's ratio values were 0.30, 0.23, 0.25, and 0.24 for the same moisture contents, respectively (Fig. 6b). The uniaxial compressive strength values were 95, 68, 61, and 66 MPa for rock with 0%, 40%, 60%, and 100% moisture content in the oil-water mixture, respectively (Fig. 6c). Similarly, in fine-medium sandstone, the Young's modulus values were 11.50, 8.10, 7.80, and 6.80 GPa for rock with 0%, 40%, 60%, and 100% moisture content in the oil-water mixture, respectively (Fig. 6a). The Poisson's ratio values were 0.17, 0.27, 0.28, and 0.34 for the same

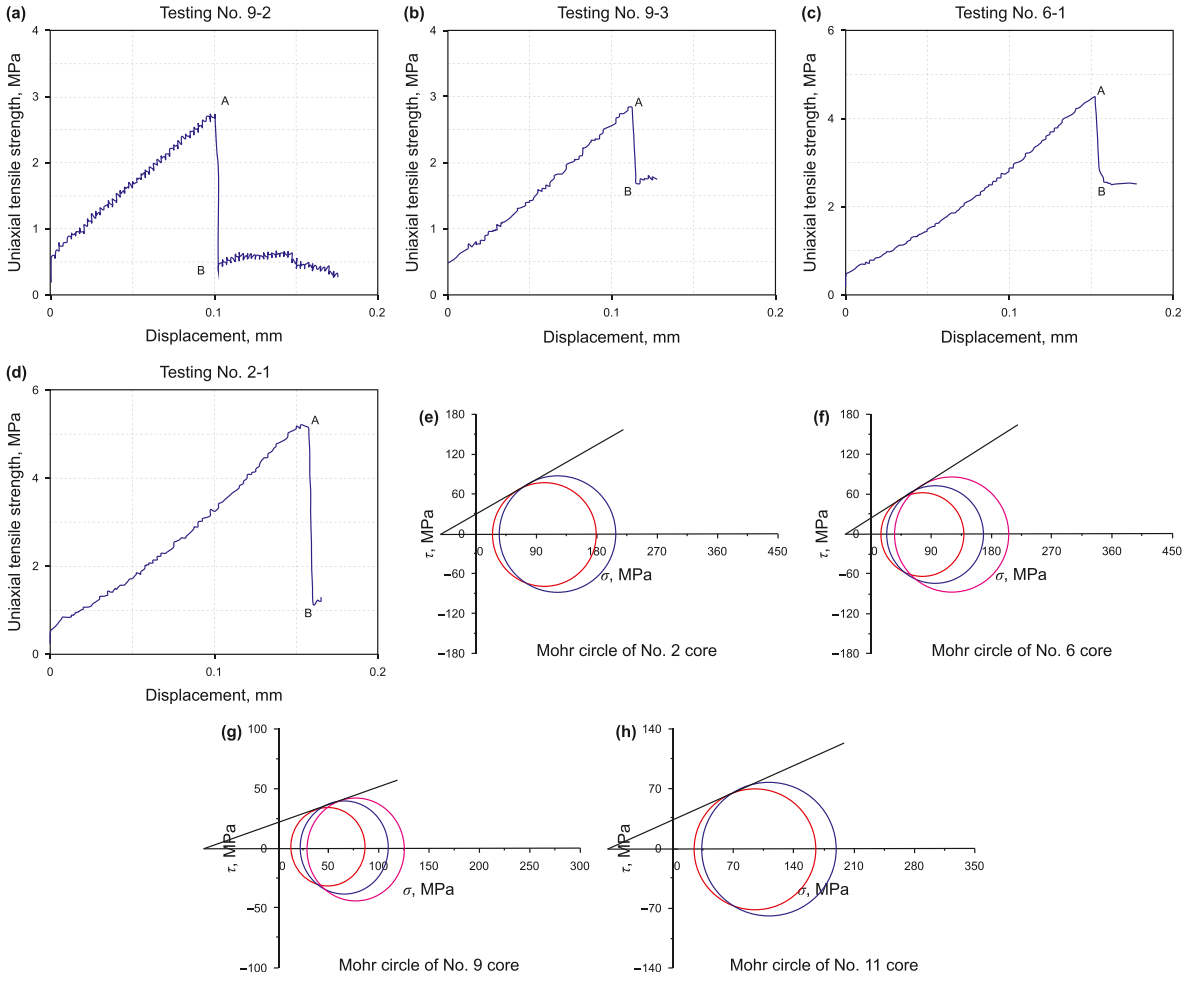

Fig. 5. The uniaxial tensile strength curve and stress-strain curves of rock mechanical testing results. **(a)**, **(b)**, **(c)**, and **(d)** show the uniaxial tensile strength curve of No. 9-2, 9-3, 6-1, and 2-1 specimen, respectively; **(e)**, **(f)**, **(g)**, and **(h)** are Mohr circle of stress-strain curve of No. 2, 6, 9, and 11 core sample, respectively.

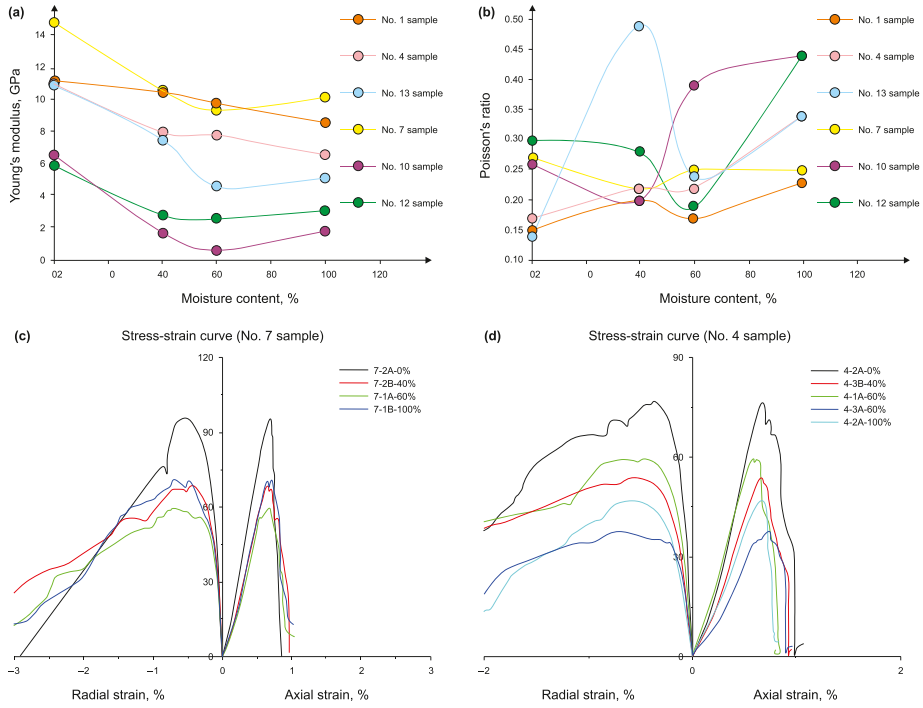

Fig. 6. The rock mechanical testing results of specimen with different moisture contents in oil-water mixture liquor. **(a)** and **(b)** show the Young's modulus variation and Poisson's ratio variation of rock with different moisture contents, respectively; **(c)** shows the stress-strain curve of No. 7 sample with different moisture contents; **(d)** refers to the stress-strain curve of No. 4 sample with different moisture contents.

moisture contents, respectively (Fig. 6b). The uniaxial compressive strength values were 77, 53, 48, and 46 MPa for rock with 0%, 40%, 60%, and 100% moisture content in the oil-water mixture, respectively (Fig. 6d). The mixing of oil and water led to increased radial and axial strain in the rock. Notably, at an oil-to-water ratio of 2:3 (60% moisture content), the uniaxial compressive strength reached its lowest value, suggesting minimal stress required for fracturing.

4.2. Calculation of rock mechanics parameters

In Well G68, with 2307 data points analyzed, Young's modulus ranged from 11.53 to 42.71 GPa, with a mean value of 19.88 GPa (Fig. 7). Poisson's ratio varied between 0.16 and 0.20, averaging at 0.18. Maximum horizontal principal stress ranged from 17.45 to 67.07 MPa, with a mean of 30.19 MPa. Minimum horizontal principal stress varied from 11.06 to 35.42 MPa, averaging 25.48 MPa. Vertical stress concentrated between 22.95 and 40.92 MPa, with a mean of 31.67 MPa. Rock density spanned 1480–2580 kg/m^3, averaging 2030 kg/m^3. Similarly, in Well G605, analyzing 15071 data points revealed Young's modulus ranging from 12.18 to 43.13 GPa, with a mean of 19.84 GPa. Poisson's ratio fluctuated between 0.16 and 0.21, averaging 0.19. Maximum horizontal principal stress ranged from 17.26 to 67.60 MPa, averaging 28.43 MPa. Minimum horizontal principal stress varied from 15.91 to 39.60 MPa, averaging 22.75 MPa. Vertical stress concentrated between 27.41 and 49.26 MPa, averaging 40.82 MPa. Rock density spanned 1720–2570 kg/m^3, averaging 2290 kg/m^3. Additionally, in Well G69, examining 35282 data points revealed Young's modulus ranging from 10.57 to 42.84 GPa, with a mean of 21.81 GPa. Poisson's ratio fluctuated between 0.16 and 0.23, averaging 0.19. Maximum horizontal principal stress ranged from 12.59 to 66.71 MPa, averaging 32.59 MPa. Minimum horizontal principal stress varied from 9.80 to 38.44 MPa, averaging 24.12 MPa. Vertical stress concentrated between 20.37 and 47.82 MPa, averaging 32.91 MPa. Rock density spanned 1730–2610 kg/m^3, averaging 2340 kg/m^3.

Consequently, well logging data was utilized to complement rock mechanical testing data for the calculation of in-situ stress and mechanical parameters. This allowed for the acquisition of continuous mechanical parameters along the longitudinal section within individual wells, and facilitated the determination of mechanical parameters related to faults. Near the fault area, a distinct pattern emerged revealing low Young's modulus values (12–15 GPa) and high Poisson's ratios (0.21–0.24). The study area exhibited significant heterogeneity, with Young's modulus ranging from 12 to 50 GPa and Poisson's ratio distributed between 0.15 and 0.24. Subsequently, an established calculation model for in-situ stress in the study area is represented by Eq. (6). Notably, where the horizontal stress difference was less than 5 MPa, effective fracturing occurred, resulting in the generation of mesh fractures (Zhou et al., 2017; Tan et al., 2023).

$$\begin{cases} \sigma_H = 0.0167h + 5.4469 \\ \sigma_h = 0.0150h + 0.9789 \\ \sigma_V = 0.0221h - 2.4647 \end{cases} \quad (6)$$

where σ_H is the horizontal maximum principal stress, MPa; σ_h is the horizontal minimum principal stress, MPa; σ_V is the vertical principal stress, MPa; h refers to the depth, m.

4.3. Results of hydraulic fracturing physical simulation experiment

In model I-1 (comprising mudstone with siltstone, argillaceous siltstone, and silty mudstone), a single cluster perforation was executed in the middle layer at a phase angle of 60°. The presence of darker fracturing fluid in the lower layer of the profile (Fig. 8a) indicated a larger rupture. Two prominent high-angle shear fractures were observed in the captured images. Over time, pore pressure increased to its peak and then gradually decreased

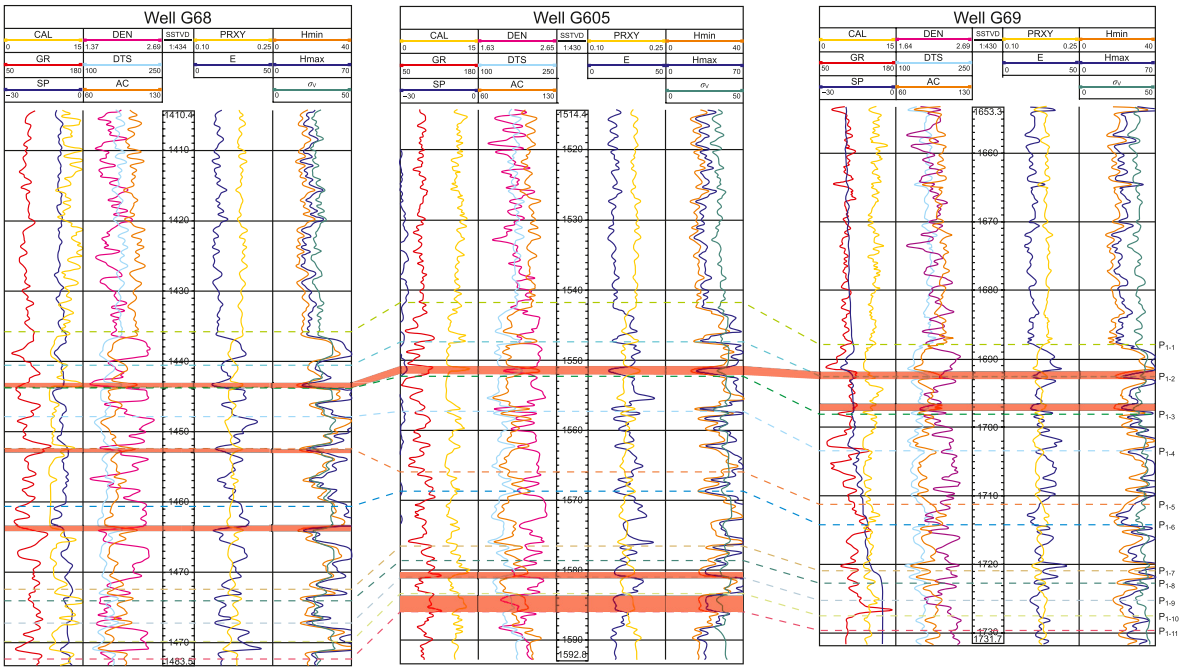

Fig. 7. The calculation results of in-situ stress and rock mechanical parameters (Young's modulus and Poisson's ratio) in typical wells (G86, G605, and G69) by well logging data.

(Fig. 9a). Fracturing fractures were initiated at the maximum initiation pressure (MIP) of 35 MPa at 0.10 h, followed by pressure decrease and re-initiation of fractures, illustrating the complex volatility between pressure and time. Moreover, displacement exhibited a positive correlation with loading time. Similarly, in model I-2, double cluster perforations were performed in the top and base layers at a phase angle of 60°. The ruptured area of fracturing fractures increased, and the extension length became longer (Fig. 8b). Pressure leakage occurred on one side due to constraint, preventing further fracturing. With increasing pressure, a stable variation period ensued, signifying fracture propagation in close natural fractures or bedding fractures (Fig. 9b). Subsequently, the maximum initiation pressure point (0.28 h) and re-initiation pressure point (0.33 h) were determined, leading to the generation of fracturing fractures. Furthermore, in model I-3, triple cluster perforations were implemented across the entire layer at a phase angle of 60°. Relatively higher rupture was observed in the top and base layers, while the middle layer exhibited lower fracturing rupture (Fig. 8c). Due to high permeability, the expansion space in argillaceous siltstone was substantial. Despite having a higher Young's modulus, the strata displayed characteristics of not easily ruptured. Numerous opened natural fractures or bedding fractures constrained the pressure-time curve, resulting in significant volatility and considerable filtration loss of fracturing fluid during fracture propagation (Fig. 9c).

In mode II-1 (comprising silty mudstone, siltstone, and mudstone), triple cluster perforations were executed across the entire layer with a phase angle of 60°. As the loading stress increased to its peak, fracturing fractures occurred, followed by a rapid decrease in fracturing pressure. Ruptures extended along the direction of maximum horizontal stress from surface U to surfaces F and B (Fig. 8d). The sandstone, with its higher Young's modulus, facilitated stress release, leading to the formation of new fracturing fractures. In model II-2, double cluster perforations were employed in the top and base layers, with four perforations in each layer. Influenced by the maximum horizontal stress, ruptures occurred on surfaces B and F. However, the propagation of fracturing fractures was hindered by the mudstone with a low Young's modulus (Fig. 8e). The double cluster perforations enhanced the rock's bearing capacity, with the maximum pore pressure it could withstand reaching 33 MPa, and the stress release time nearly doubling (Fig. 9d). In model II-3, triple cluster perforations were conducted across the entire layer, with three perforations in the top and base layers and two perforations in the middle layer, at a phase angle of 45°. Due to the perforation phase and number restrictions, the maximum perforation pressure decreased, and the rupture time increased. The extension of fracturing fractures was relatively subdued on surfaces B and F (Fig. 8f).

In model III-1 (consisting of mudstone, sandstone, and mudstone), triple cluster perforations were executed across the entire layer, with two perforations in each layer. Fracturing fractures occurred in three directions, indicating a middle to high dip angle (Fig. 8g). The pore pressure increased slowly to its peak (48 MPa), followed by a rapid decrease after fracturing fractures formed (Fig. 9e). In model III-2, triple cluster perforations were conducted across the entire layer, with four perforations in each layer. Fracturing fractures generated by the maximum horizontal stress were impeded by fractures formed by the minimum horizontal stress (Fig. 8h). The increased perforations influenced the internal mechanical properties, elongating the time to reach the pressure peak (Fig. 9f). In model IV (comprising silty mudstone, siltstone, and mudstone), double cluster perforations were executed in the top and base layers at a phase angle of 60°. Fracturing fractures initiated in the center and then extended to the bottom (Fig. 8i), demonstrating diastrophism across different lithologies.

4.4. Distribution characteristics of in-situ stress

4.4.1. Distribution characteristics of in-situ stress without perforations

The rock mechanical parameters and loading conditions aligned with the physical simulation of hydraulic fracturing (Fig. 3 and Table 5). Notably, positive values in the ANSYS software indicated

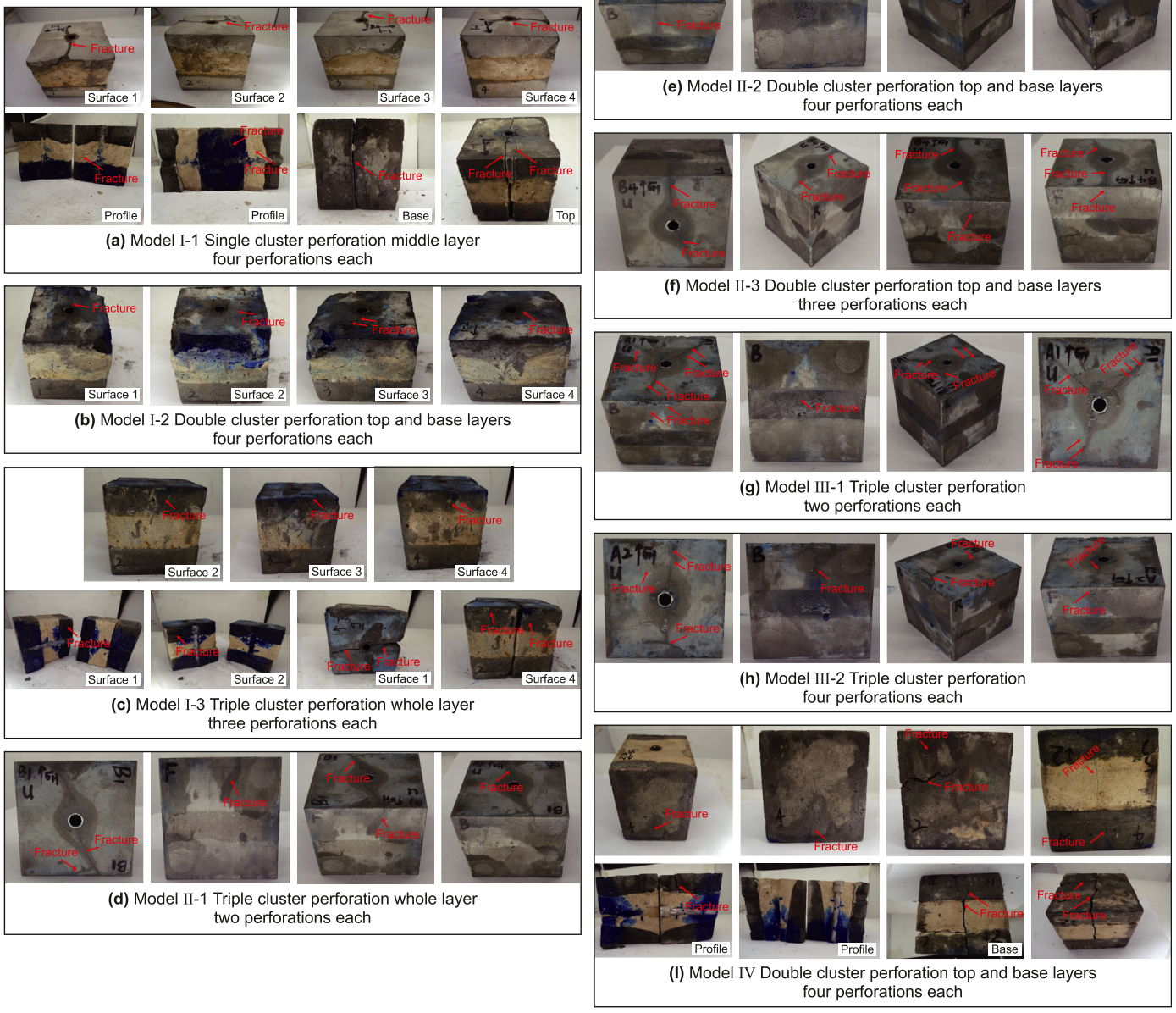

Fig. 8. The results of hydraulic fracturing physical simulation experiment. **(a)** is the single cluster perforation in middle layer in model I in Fig. 4; **(b)** refers to the double cluster perforations in top and base layers in model I; **(c)** shows the triple cluster perforation in whole layer in model I; **(d)** is the triple cluster perforation in whole layer in model II; **(e)** refers to the double cluster perforations in top and base layers in model II; **(f)** indicates the double cluster perforations in model II; **(g)** is the triple cluster perforation with three perforations each in model III; **(h)** is the triple cluster perforation with four perforations each in model III; **(i)** shows the double cluster perforations in top and base layers in model IV. Where surface 1 and 2 are the normal directions of horizontal minimum principal stress; surface 3 and 4 are the normal directions of horizontal maximum principal stress; surface R and L are the normal directions of horizontal minimum principal stress; surface B and F are the normal directions of horizontal maximum principal stress.

tensile stress, while negative values represented compressive stress. Though contrary to geological representation, this did not hinder research on the distribution characteristics of in-situ stress. According to the simulated results (Fig. 10a, b, c, and d), the magnitude of the minimum principal stress was primarily distributed between 14.60 and 19.80 MPa, indicating compressive stress. The highest minimum principal stress was concentrated in the mudstone with silty mudstone and siltstone (18.70–19.80 MPa), especially along lithologic interfaces, signifying easily fracturing areas. Notably, the middle principal stress showed a smaller value along the x-direction (perpendicular to the direction of maximum principal stress) and the largest value along the y-direction (parallel to the direction of maximum principal stress) (Fig. 10b). The maximum principal stress magnitude was primarily distributed between 30.20 and 32.40 MPa, also exhibiting compressive stress (Fig. 10c). The highest maximum principal stress values were observed in argillaceous siltstone (30.90–32.40 MPa), followed by mudstone with siltstone (30.40–31.40 MPa), with silty mudstone showing the least values (30.20–31.10 MPa). Stress intensity was primarily concentrated between 11.20 and 17.00 MPa (Fig. 10d),

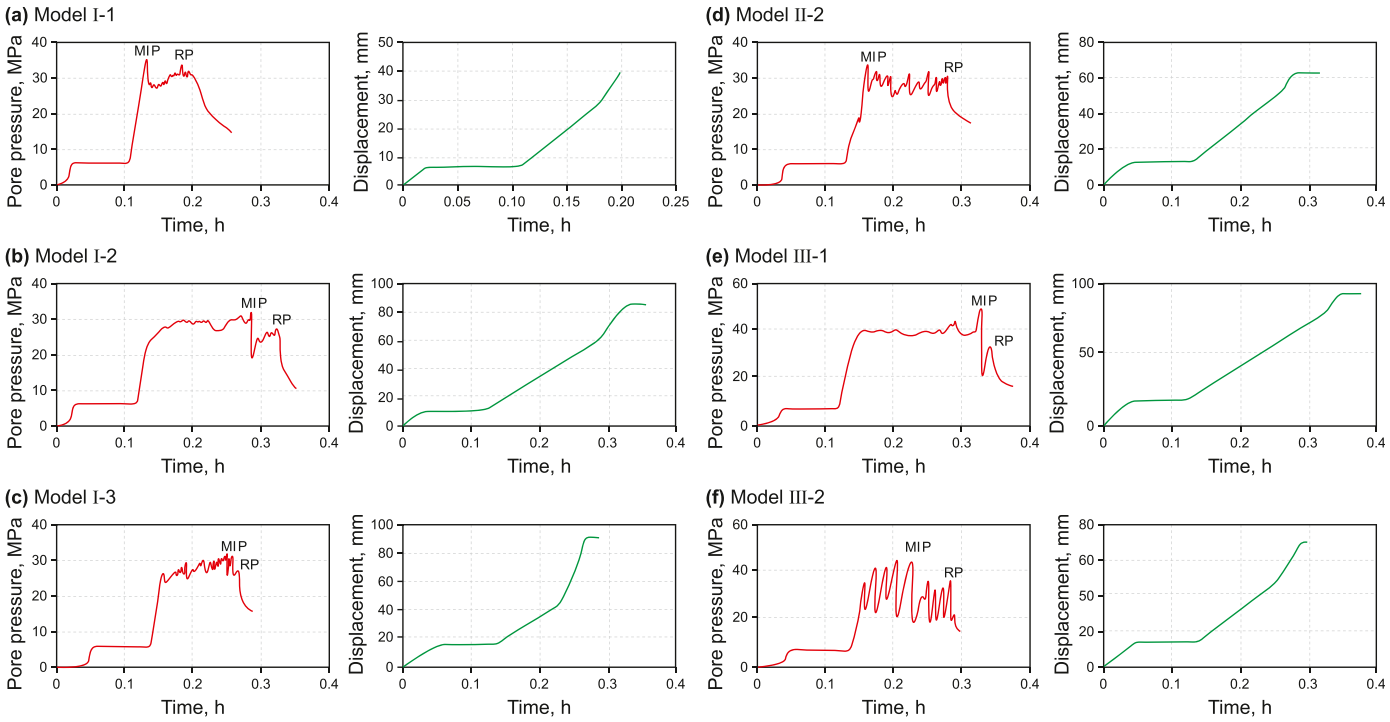

Fig. 9. The pore pressure and displacement of perforation in different models in the study area. **(a)** is the pore pressure and displacement curve in model I-1; **(b)** shows pore pressure and displacement curve in model I-2; **(c)** refers to the pore pressure and displacement curve in model I-3; **(d)** shows the pore pressure and displacement curve in model II-2; **(e)** refers to the pore pressure and displacement curve in model III-1; **(f)** shows the pore pressure and displacement curve in model III-2; where MIP refers to the maximum initiation pressure; RP shows the re-initiation pressure.

showing an inverse distribution trend compared to the minimum principal stress. Higher stress intensity was observed in argillaceous siltstone (13.80–17.00 MPa), with lower values in mudstone with siltstone and silty mudstone (11.20–14.40 MPa). Notably, stress intensity near lithologic interfaces exhibited significant differences (abrupt change values), indicating a strong potential for fracture production in argillaceous siltstone.

Similarly, according to the simulated results (Fig. 10e, f, g, and h), in the transverse lithologic segment, the magnitude of the minimum principal stress was primarily distributed between 7.01 and 0.00 MPa, indicating compressive stress. Additionally, the minimum principal stress exhibited a tensile value of 0.00–5.87 MPa (Fig. 10e). Particularly, the minimum principal stress displayed two abrupt stress environments near the lithologic interface, making fracture generation prone in the argillaceous siltstone near the interface. The smallest value of the middle principal stress was distributed in the mudstone (21.70–23.60 MPa) (Fig. 10f). The magnitude of the maximum principal stress was primarily distributed between 28.90 and 39.30 MPa with compressive stress (Fig. 10g). The largest maximum principal stress was near the interface in argillaceous siltstone (37.00–39.30 MPa), while the value in the mudstone was the least (28.90–30.10 MPa). The magnitude along the lithologic interface was significant, indicating a tendency to rupture easily. Stress intensity was primarily concentrated between 23.90 and 43.90 MPa (Fig. 10h), showing an opposite distribution trend compared to the minimum principal stress. Higher stress intensity was distributed in the argillaceous siltstone (32.80–43.90 MPa), with lower values in the mudstone and silty mudstone (23.90–32.80 MPa). Especially, the largest value of stress intensity (39.50–43.90 MPa) was concentrated near the lithologic interface in the argillaceous siltstone, indicating a high tendency for rupture.

4.4.2. Distribution characteristics of in-situ stress by single cluster perforation

According to the simulated results of in-situ stress in vertical lithologic stratification due to single cluster perforation (Fig. 11a), the magnitude of the minimum principal stress ranged between 4.51 and 24.66 MPa. The middle principal stress values were primarily between 0.00 and 29.10 MPa. The magnitude of the maximum principal stress was mainly distributed between 7.25 and 46.60 MPa, with lower values (7.25–26.90 MPa) concentrated near the cluster perforation area. Stress intensity was concentrated between 2.11 and 38.50 MPa, showing good consistency with the calculated results (Fig. 7). Total deformation was mainly distributed between 0.00 and 60.85 μm, indicating significant deformation (30.49–60.99 μm) near the cluster perforation. The magnitude of equivalent elastic strain indicated higher values ($15.61–31.82\times10^{-4}$) near the cluster perforation. The noticeable differences and abrupt variations revealed the capacity to rupture and generate more fracturing fractures near the cluster perforation. Overall, with increasing distance from the cluster hole, the magnitude of the maximum, middle, and minimum principal stress increased. A similar variation tendency was identified among stress intensity, equivalent elastic strain, and equivalent (von-Mises) stress, with a sharp decrease along the *y* direction (parallel to the direction of maximum principal stress) and a slower decrease along other directions.

Similarly, in the transverse lithologic segment (Fig. 11b), the magnitude of the minimum principal stress was distributed between 0.00 and 30.10 MPa. The value of the middle principal stress ranged primarily between 0.93 and 30.92 MPa. The magnitude of the maximum principal stress performed lower values (16.30–34.20 MPa) in the area near the cluster perforation. Stress intensity was concentrated between 1.50 and 45.08 MPa, indicating three directions prone to rupture. Total deformation showed significant deformation (4.59–8.25 μm) near the cluster perforation.

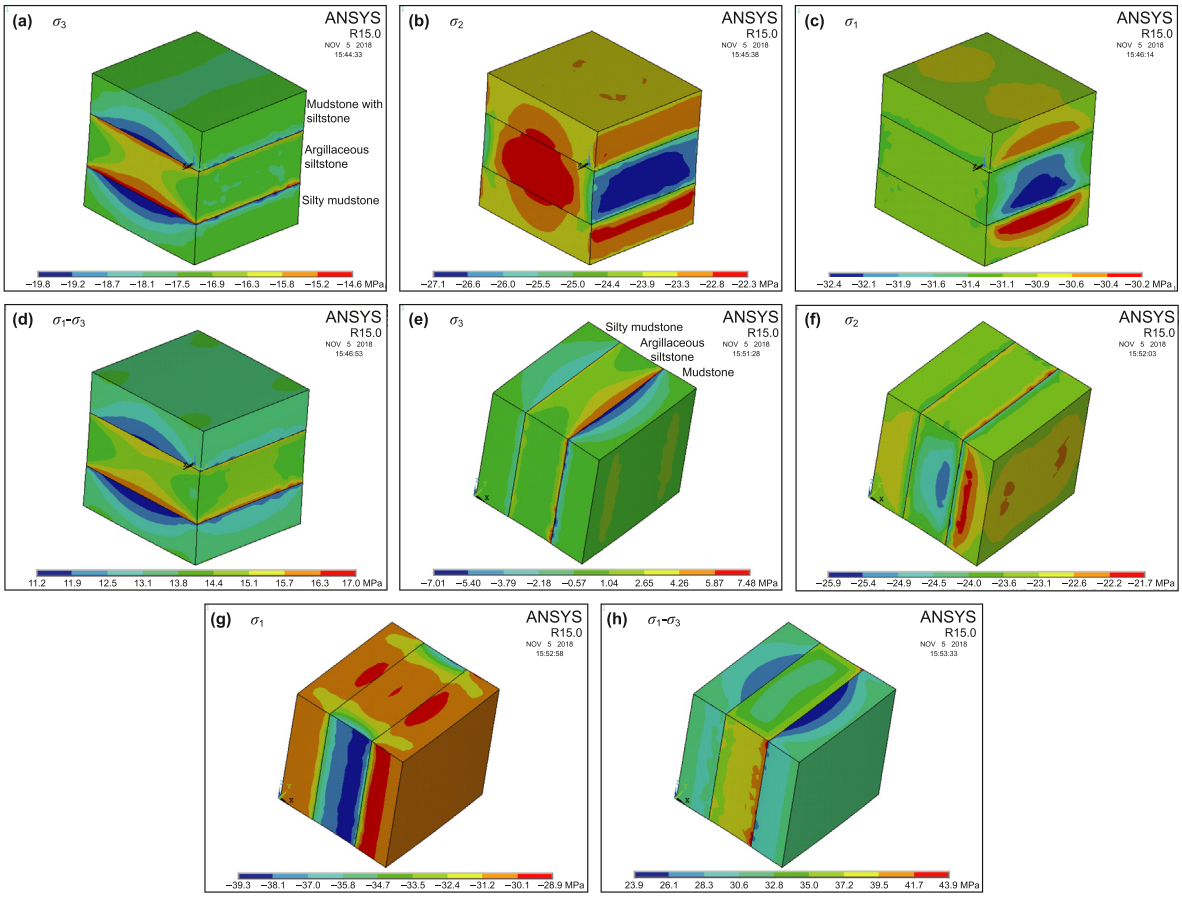

Fig. 10. The 3-D distribution characteristics of in-situ stress in two different lithological combinations without perforations. **(a)**, **(b)**, **(c)**, **(d)** refer to the minimum principal stress, middle principal stress, maximum principal stress, and stress intensity in vertical lithologic stratification, respectively; **(e)**, **(f)**, **(g)**, **(h)** show the minimum principal stress, middle principal stress, maximum principal stress, and stress intensity in transverse lithologic segment, respectively.

The deformation degree was lower than that in the vertical lithologic stratification model. The value of the equivalent (von-Mises) stress was mainly distributed between 1.46 and 45.83 MPa, showing a similar characteristic to the equivalent elastic strain. Consequently, stress intensity, equivalent elastic strain, and equivalent (von-Mises) stress showed the largest values in the cluster perforation area, with similar distribution characteristics along the interface. Total deformation increased slowly along the positive *Y*-axis and decreased slowly along the negative *Y*-axis.

Additionally, in argillaceous siltstone (Fig. 11c), the magnitude of the minimum principal stress was distributed between 0.00 and 23.82 MPa. The magnitude of the maximum principal stress was mainly distributed between 13.85 and 48.77 MPa, with lower values (13.85–31.31 MPa) concentrated in the area near the cluster perforation. Stress intensity was concentrated between 2.19 and 45.14 MPa, indicating three directions prone to rupture. Total deformation was mainly distributed between 0.00 and 66.81 μm, with significant deformation (29.69–44.54 μm) near the cluster perforation. The magnitude of equivalent elastic strain ranged primarily between 0.00011543 and 0.004894, with higher values ($11.34–23.87\times10^{-4}$) near the cluster perforation. The value of the equivalent (von-Mises) stress was mainly distributed between 2.07 and 44.38 MPa. Similarly, stress intensity, equivalent elastic strain, and equivalent (von-Mises) stress showed the largest values in the cluster perforation area. Total deformation increased slowly along the positive *Y*-axis and decreased slowly along the negative *Y*-axis. In conclusion, the area near the cluster perforation indicated a large stress difference, strong deformation, and high elastic strain compared to other areas, showing a better capacity to be fractured and generate fracturing fractures.

4.4.3. Distribution characteristics of in-situ stress by double cluster perforations

According to the simulated results of in-situ stress in vertical lithologic stratification by double cluster perforations (Fig. 12a), lower compressive values (0.00–17.09 MPa) of the minimum principal stress were concentrated near the cluster hole. Little tensile stress (0.00–2.06 MPa) was identified along the cluster perforation, indicating the ability to generate opening fractures. The magnitude of maximum principal stress was mainly distributed between 0.00 and 57.6 MPa. Tensile stress (0.00–5.03 MPa) was distributed near the cluster perforation area, indicating the capacity to form tensile fractures. Stress intensity was concentrated between 2.28 and 49.77 MPa, showing good agreement with the calculated results from well logging data (Fig. 7). Total deformation was mainly distributed between 0.00 and 88.04 μm, indicating strong deformation (58.69–78.26 μm) near the cluster perforation. The magnitude of equivalent elastic strain ranged primarily between 1.27×10^{-4} and 3.03×10^{-4}. The significant difference and abrupt variation indicated the capacity to be ruptured and generate more fracturing fractures near the cluster perforation, revealing three significant directions prone to rupture. Overall, as the distance from the cluster hole increased, the magnitude of the minimum principal stress initially increased and then decreased. A

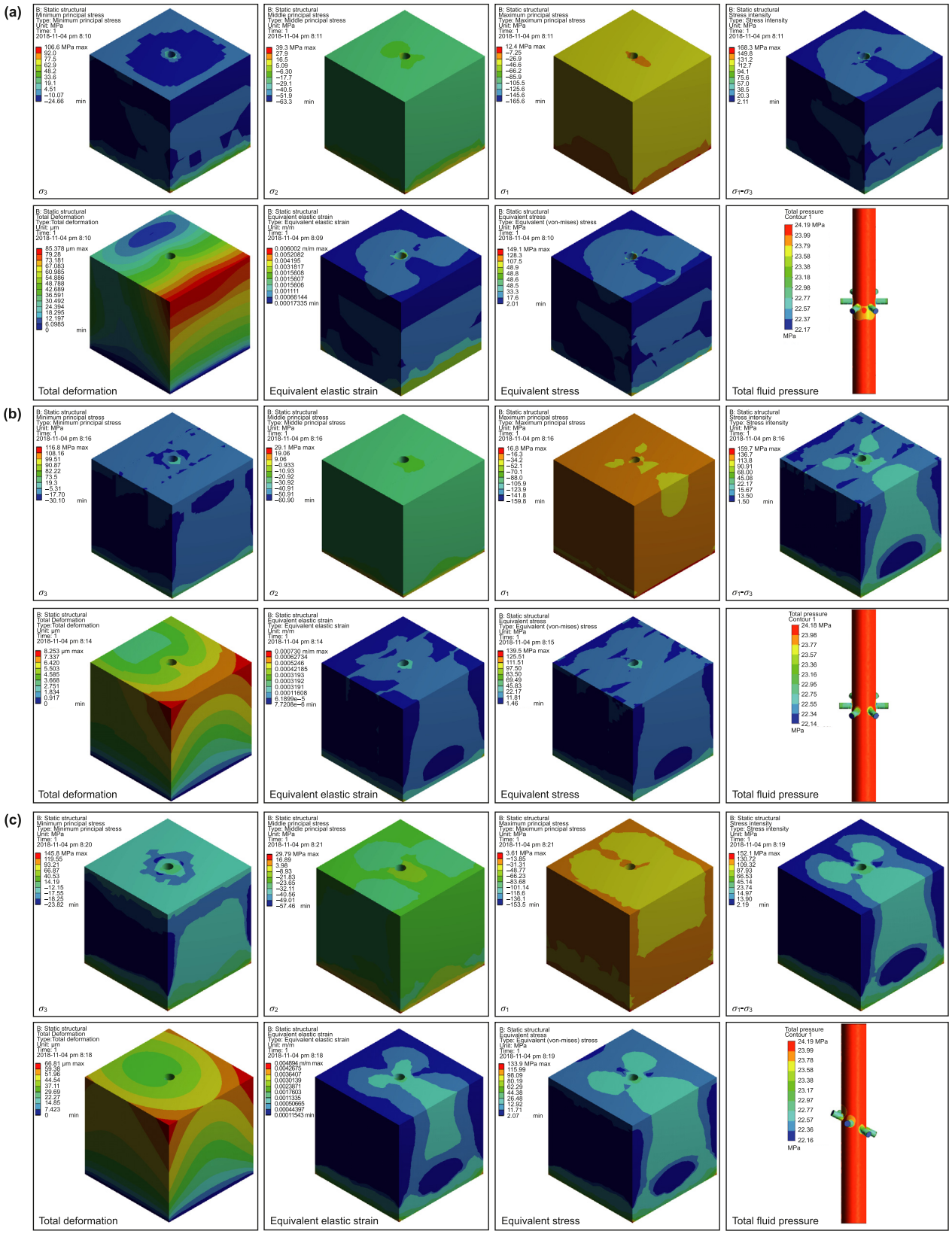

Fig. 11. The 3-D distribution characteristics of in-situ stress in different lithological combinations during the hydraulic fracturing physical experiment by single cluster perforation. **(a)** is the in-situ stress characteristic in vertical lithologic stratification; **(b)** shows the in-situ stress characteristic in transverse lithologic segment; **(c)** refers to the in-situ stress characteristic in argillaceous siltstone.

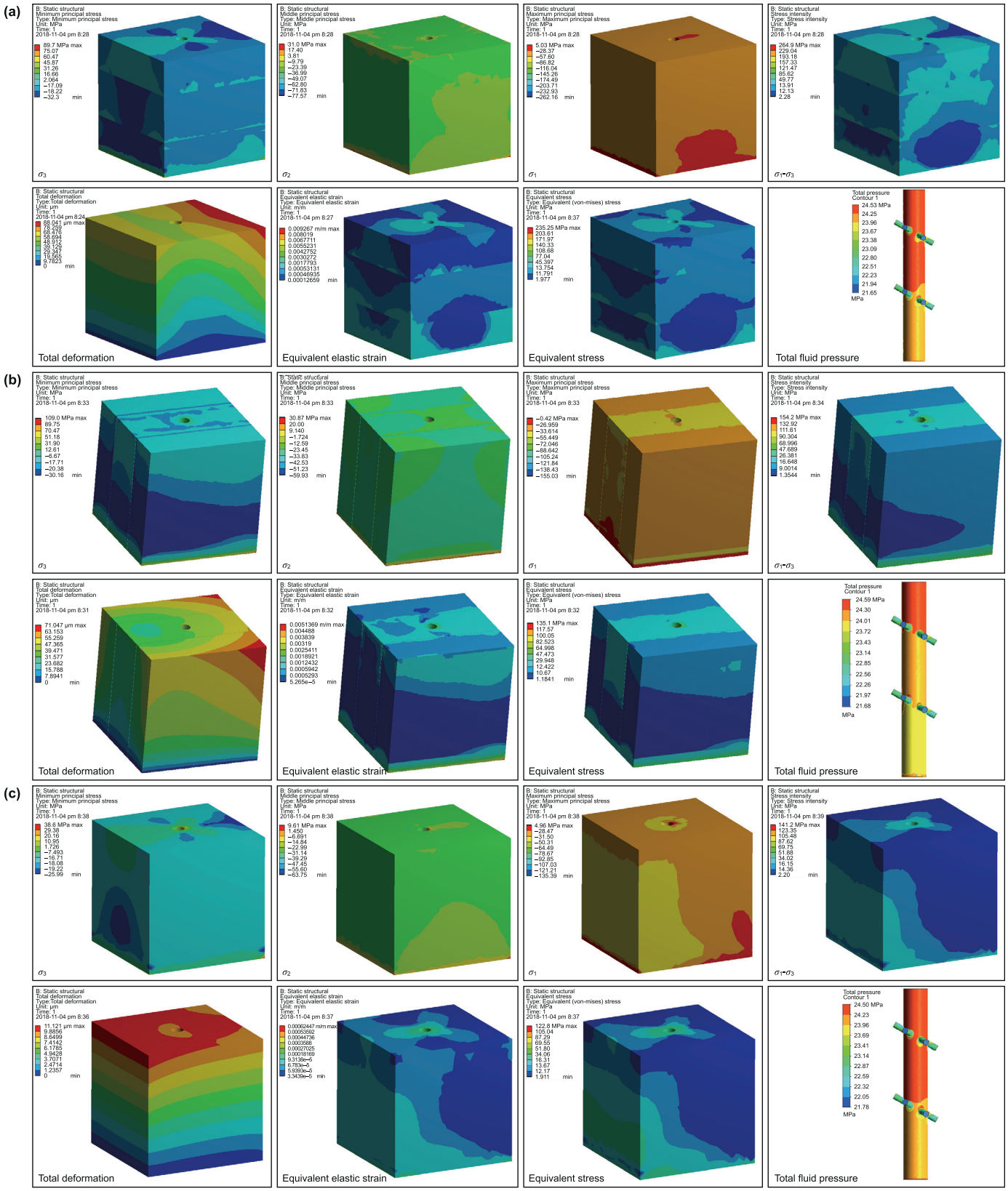

Fig. 12. The 3-D distribution characteristics of in-situ stress in different lithological combinations during the hydraulic fracturing physical experiment by two cluster perforations. **(a)** is the in-situ stress characteristic in vertical lithologic stratification; **(b)** shows the in-situ stress characteristic in transverse lithologic segment; **(c)** refers to the in-situ stress characteristic in argillaceous siltstone.

similar variation tendency was observed among stress intensity, equivalent elastic strain, and equivalent (von-Mises) stress, indicating three predominant directions for generating fracturing fractures.

In the transverse lithologic segment (Fig. 12b), lower compressive values (0.00–6.67 MPa) of the minimum principal stress were concentrated in the area near the cluster hole. Tensile stress (0.00–12.67 MPa) was identified along the cluster perforation, showing a good capacity to form fracturing fractures. The magnitude of maximum principal stress was mainly distributed between 0.42 and 55.45 MPa, indicating an optimized direction for rupture. Stress intensity was concentrated between 1.35 and 47.69 MPa, showing good consistency with the calculated results from well logging data (Fig. 7). Total deformation showed strong deformation (31.58–47.37 μm) near the cluster perforation. The significant difference and abrupt variation indicated the capacity to be ruptured and generate more fracturing fractures near the cluster perforation, revealing three significant directions for rupture. The value of the equivalent (von-Mises) stress was mainly distributed between 1.1841 and 47.47 MPa, showing good agreement with the equivalent elastic strain. A similar variation tendency was observed among stress intensity, equivalent elastic strain, and equivalent (von-Mises) stress, indicating a larger magnitude in the siltstone and lower values in the silty mudstone and mudstone.

In the argillaceous siltstone model (Fig. 12c), lower compressive values (0.00–7.49 MPa) of the minimum principal stress were concentrated in the area near the cluster hole, indicating three directions prone to generate fracturing fractures. Tensile stress (0.00–10.95 MPa) was identified along the cluster perforation, indicating an ability to form opening fractures. The magnitude of maximum principal stress was mainly distributed between 0.00 and 50.31 MPa. Tensile stress (0.00–4.96 MPa) was also distributed near the cluster perforation area, revealing the ability to form tensile fractures. Three optimized directions prone to rupture were distinguished by higher stress intensity (16.15–34.02 MPa). Total deformation was mainly distributed between 0.00 and 11.12 μm, with strong deformation (8.65–11.12 μm) near the cluster perforation. The equivalent elastic strain in the argillaceous siltstone was smaller than that in the vertical lithologic stratification and transverse lithologic segment. Comprehensively, increasing the distance from the cluster hole, the magnitude of the minimum principal stress initially increased and then decreased. A similar variation tendency was identified among stress intensity, equivalent elastic strain, and equivalent (von-Mises) stress, indicating three predominant directions to generate fracturing fractures. The largest values were identified along the cluster perforations, indicating the capacity to generate fracturing fractures. The total indicated larger values on the top surface and decreased along the negative direction of the *y*-axis (parallel to the direction of maximum principal stress).

5. Discussions

5.1. Distribution characteristics of hydraulic fractures during the FENS

To analyze the developmental characteristics of hydraulic fractures, the fracture density and aperture were quantitatively calculated based on simulated in-situ stress. Constrained by the principal strain and corresponding principal stress, the strain energy per unit volume was determined. Subsequently, the magnitude of elastic strain energy in the entire rock was obtained (Ren et al., 2019; Feng et al., 2019; Ren et al., 2021). Two rupture criteria situations were distinguished as follows.

(1) When $\sigma_3 > 0$, according to the Coulomb-Mohr criterion, the fracture volume density and linear density were determined through Eqs. (7) and (8).

$$D_{vf} = \frac{1}{2E(J_0 + \sigma_3 b)}\left[\sigma_1^2 + \sigma_2^2 + \sigma_3^2 - 2\mu(\sigma_1\sigma_2 + \sigma_2\sigma_3 + \sigma_1\sigma_3) - 0.85^2\sigma_p^2 + 2\mu(\sigma_2 + \sigma_3)\sigma_p\right] \tag{7}$$

$$D_{lf} = \frac{2D_{vf}L_1L_3\sin\theta\cos\theta - L_1\sin\theta - L_3\cos\theta}{L_1^2\sin^2\theta + L_3^2\cos^2\theta} \tag{8}$$

where D_{vf} is the fracture volume density, m^2/m^3; J_0 refers to the required surface energy without pressure, J/m^2; E is the rock's Young's modulus, MPa; μ shows the rock Poisson's ratio, dimensionless; σ_1, σ_2, σ_3 refer to the minimum, middle, and maximum principal stress, respectively, MPa; b is the fracture aperture, m; σ_p refers to the rock rupture stress, MPa; D_{lf} is the fracture linear density, m^{-1}; L_1 and L_3 are the characterized unit lengths along the σ_1 and σ_3 orientations, m; and θ refers to the rock rupture angle, °.

(2) When $\sigma_3 < 0$, based on the Griffith criterion, two sub situations were divided:

When $\sigma_1+3\sigma_3 > 0$, the fracture volume density and linear density were calculated through Eqs. (9) and (10):

$$D_{vf} = \frac{1}{2(J_0 + \sigma_3 b)}\left[\sigma_1^2 + \sigma_2^2 + \sigma_3^2 - 2\mu(\sigma_1\sigma_2 + \sigma_2\sigma_3 + \sigma_1\sigma_3) - \sigma_t^2\right] \tag{9}$$

$$D_{lf} = \frac{2D_{vf}L_1L_3\sin\theta\cos\theta - L_1\sin\theta - L_3\cos\theta}{L_1^2\sin^2\theta + L_3^2\cos^2\theta} \tag{10}$$

where σ_t shows the rock tensile strength, MPa.

When $\sigma_1+3\sigma_3 \le 0$, the fracture volume density and linear density were obtained through Eq. (11).

$$D_{lf} = D_{vf} = \frac{1}{2(J_0 + \sigma_3 b)}\left[\sigma_1^2 + \sigma_2^2 + \sigma_3^2 - 2\mu(\sigma_1\sigma_2 + \sigma_2\sigma_3 + \sigma_1\sigma_3) - \sigma_t^2\right] \tag{11}$$

The fracture aperture was calculated through Eq. (12).

$$b = \frac{|\varepsilon_3| - |\varepsilon_0|}{D_{lf}} \tag{12}$$

where ε_0 refers to the maximum elastic strain of rock affordability.

According to the calculated results (Fig. 13), in the vertical lithologic stratification by single cluster perforation, the fracture aperture indicated higher values (0.12–0.25 mm) in the argillaceous siltstone and lower values (0.00–0.15 mm) in the mudstone with siltstone and silty mudstone (Fig. 13a). The fracture linear density showed relatively higher values (0.30–0.50 fractures/m) in the silty mudstone and lower values (0.00–0.30 fractures/m) in the mudstone with siltstone and argillaceous siltstone. The significant difference in fracture aperture and linear density near the cluster perforations indicated two optimized directions for rupture. For the transverse lithologic segment model, the fracture aperture indicated larger magnitudes (0.10–0.25 mm) in the mudstone with siltstone and silty mudstone (Fig. 13b). Relatively lower values

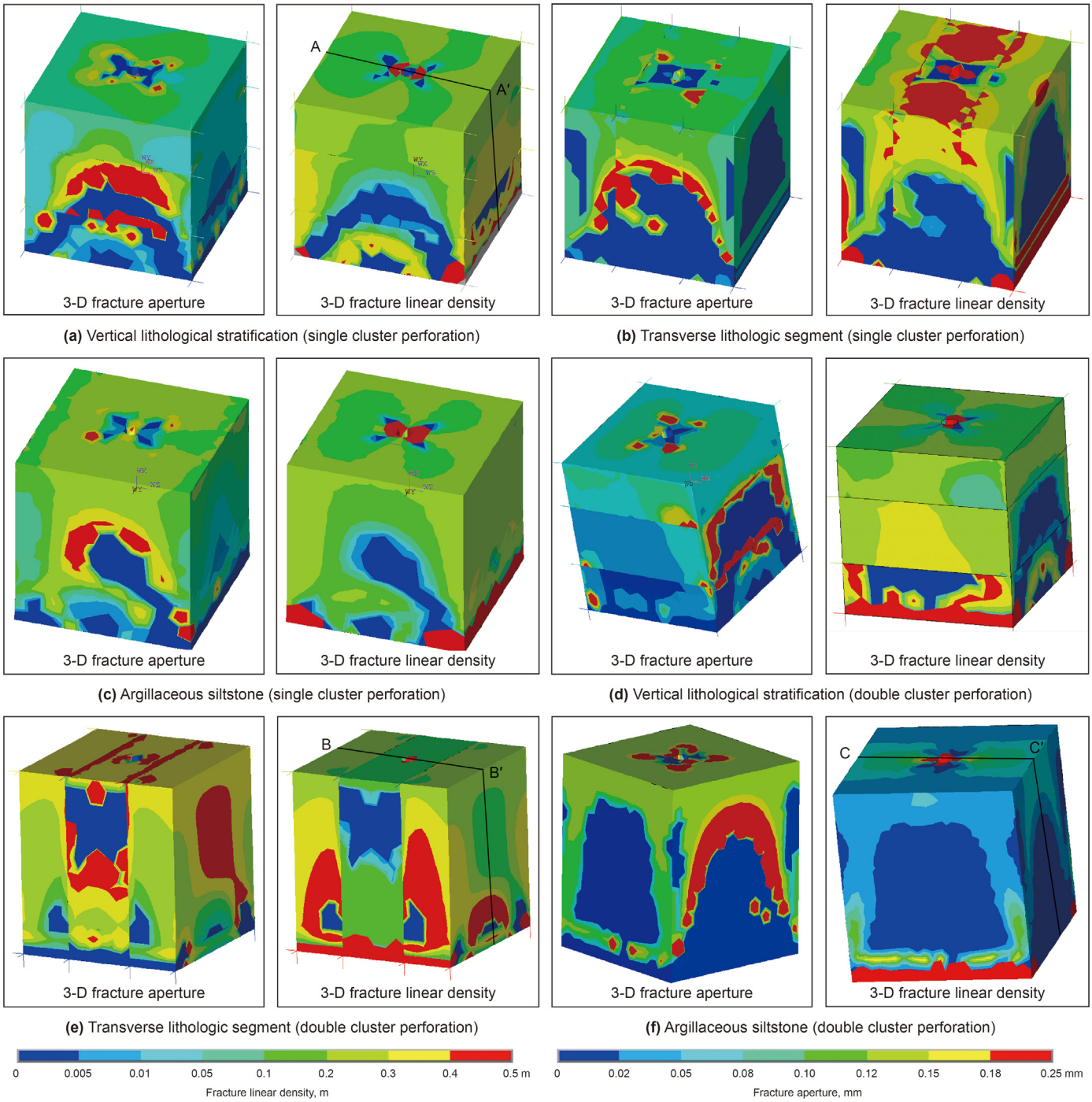

Fig. 13. The 3-D distribution characteristics of fracture aperture and linear density in different lithological combinations during the hydraulic fracturing physical experiment by different cluster perforations. **(a)** is the fracture aperture and linear density of vertical lithologic stratification by single cluster perforation; **(b)** shows the fracture aperture and linear density of transverse lithologic segment by single cluster perforation; **(c)** refers to the fracture aperture and linear density of argillaceous siltstone by single cluster perforation; **(d)** shows the fracture aperture and linear density of vertical lithologic stratification by double cluster perforations; **(e)** is the fracture aperture and linear density of transverse lithologic segment by double cluster perforations; **(f)** refers to the fracture aperture and linear density of argillaceous siltstone by double cluster perforations.

(0.00–0.10 mm) of fracture aperture were distributed in the argillaceous siltstone. The relatively higher fracture linear density (0.05–0.30 fractures/m) was primarily concentrated in the mudstone with siltstone, while the largest values (0.40–0.50 fractures/m) of fracture linear density were distributed in the silty mudstone, with the least value in the middle part of the argillaceous siltstone and silty mudstone. Similarly, the area near the cluster perforations indicated a good capacity to generate new hydraulic fractures due to the abrupt variation of fracture aperture and linear density. In the argillaceous siltstone model, higher fracture apertures (0.18–0.25 mm) were primarily concentrated in the middle part, with lower fracture apertures (0.00–0.18 mm) distributed in the upper and lower sides (Fig. 13c). The area near the cluster perforations indicated the largest fracture linear density (0.40–0.50 fractures), showing the capacity to easily form new fractures.

The fracture aperture within the vertical lithologic stratification, as influenced by double cluster perforations, demonstrated larger values (0.12–0.25 mm) in proximity to the cluster perforations (Fig. 13d). Within the mudstone with siltstone, a relatively higher aperture range (0.08–0.18 mm) was observed, while a relatively lower aperture range (0.00–0.05 mm) was primarily concentrated in the argillaceous siltstone and silty mudstone. The highest fracture linear density (0.40–0.50 fractures/m) was found in the silty mudstone. Moreover, the significant variation in fracture aperture and linear density near the cluster perforations indicated a notable propensity for rupture. In the transverse lithologic segment model, fracture aperture was notably larger (0.18–0.25 mm) around the cluster perforations, signifying a greater propensity for rupture (Fig. 13e). Siltstone exhibited the largest disparity in fracture aperture, with relatively higher values in its middle section. Fracture linear density showed relatively higher values (0.10–0.50 fractures/m) in the mudstone with siltstone and mudstone, with the region near the cluster perforations demonstrating particularly high density (0.40–0.50 fractures/m). Furthermore, in the argillaceous siltstone model, fracture aperture was notably high (0.10–0.25 mm) in the upper part, peaking near the cluster perforations (0.20–0.25 mm) (Fig. 13f). Similarly, fracture linear density indicated high values (0.05–0.30 fractures/m) around the cluster perforations. The substantial differences and abrupt variations near the cluster perforations underscored the notable potential for generating new fracturing fractures.

Consequently, a comparison between the hydraulic fracturing physical experiment and finite element numerical simulation was undertaken (Fig. 14). In the vertical lithologic stratification model with single cluster perforation, the rock tended to generate fractures towards the base layer at a low to middle angle (30–60°) (Fig. 14a). The rupture direction observed during the physical experiment exhibited a similar characteristic to that in the FENS. In the transverse lithologic segment model with double cluster perforations, rupture was inclined to be generated along a low to middle angle (15–60°) towards the base layer from the lower cluster perforation area (Fig. 14b). In the argillaceous siltstone model, hydraulic fractures were inclined to form along a middle angle (30–60°) towards the upper layer from the lower cluster perforation area (Fig. 14c). In summary, the calculated results of FENS exhibited good agreement with those observed during the hydraulic fracturing physical simulation. Ruptures were prone to form near the cluster perforations, with the rupture direction indicating a low to middle angle (15–60 °).

5.2. Dynamic evolution of the fracturing fracture system during the physical experiment

In order to analyze the dynamic evolution of the fracturing fracture system, AE testing (sensor) was conducted on all physical experiment samples. Unfortunately, only six specimens succeeded, and the corresponding fracturing fracture characteristics are depicted in Figs. 15–20. Due to the constraint imposed by the single cluster perforation in the middle layer, the fracturing fracture ruptured in the central area of the rock, indicating a fracturing direction along the minimum principal stress (Fig. 15a). Subsequently, the fracturing fracture gradually extended towards the upper-left direction in the *X-Z* plane, revealing better rupture ability in the upper layer compared to the lower layer (Fig. 15b). Moreover, conjugate shear fractures developed, predominantly extending along the NW-SE (300°–330°) direction and weakly along the NE-SW (40°–60°) direction in the *X-Z* plane (Fig. 15c). As a result, a complex network of fracturing fractures was formed, indicating good rupture ability in layers with relatively higher Young's modulus and large extension distance along the *X-Z* plane (Fig. 15d).

Similarly, controlled by the double cluster perforations in the upper and lower layers, fracturing fractures were generated throughout the entire rock, indicating a fracturing direction along the acute angle with the minimum principal stress (Fig. 16a). Subsequently, an optimized fracturing fracture along the NW-SE (310°–330°) direction in the *X-Z* plane was formed, indicating a strong rupture capacity throughout the layer (Fig. 16b). This was followed by the sequential development of fracturing fractures and

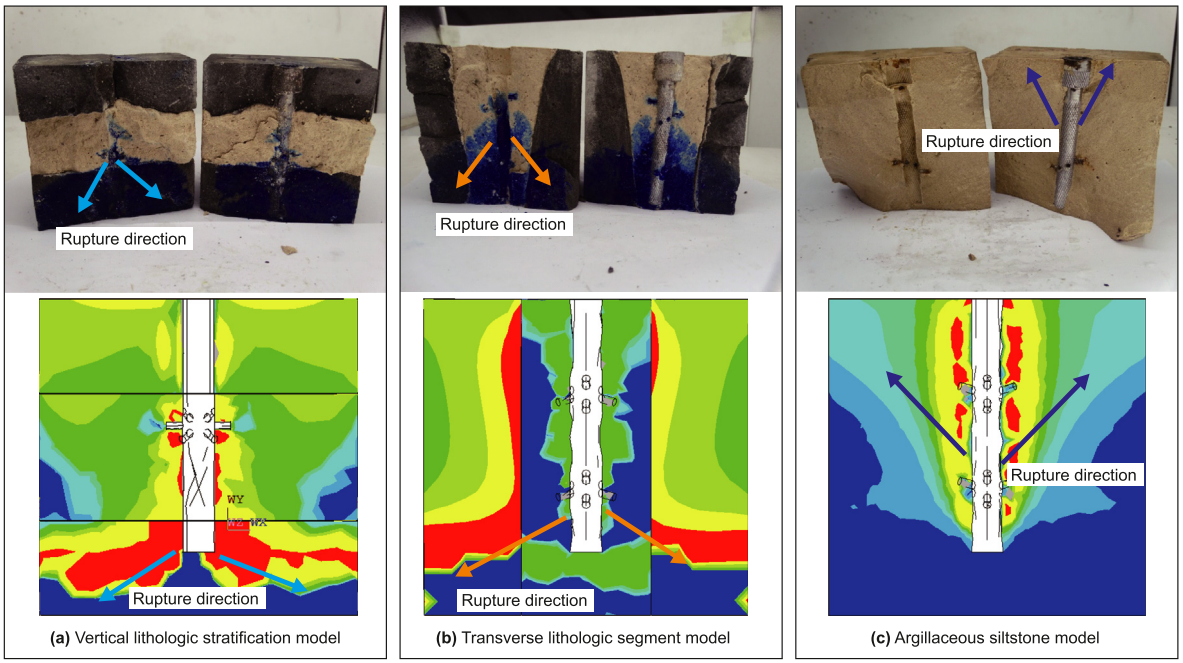

Fig. 14. The comparison of the physical experiment and finite element numerical simulation. **(a)** is the vertical lithologic stratification model by single cluster perforation; **(b)** shows the transverse lithologic segment model by double cluster perforations; **(c)** refers to the argillaceous siltstone model by double cluster perforations.

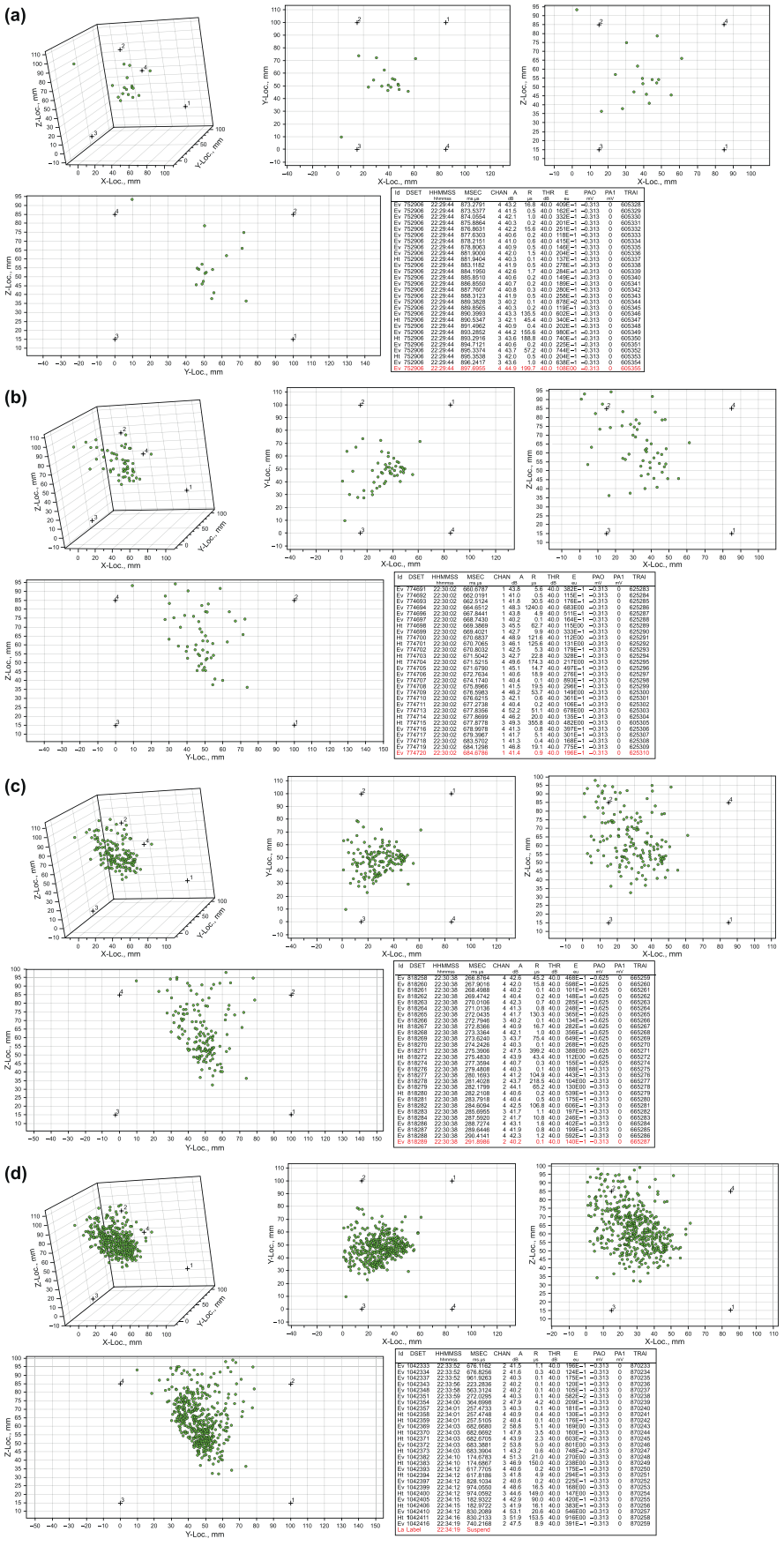

Fig. 15. The testing results of acoustic emission in Model I-1 in Fig. 8. **(a)** is the initial rupture stage; **(b)** and **(c)** show the intermediate rupture stage (0.5 and 0.75); **(d)** refers to the final rupture stage.

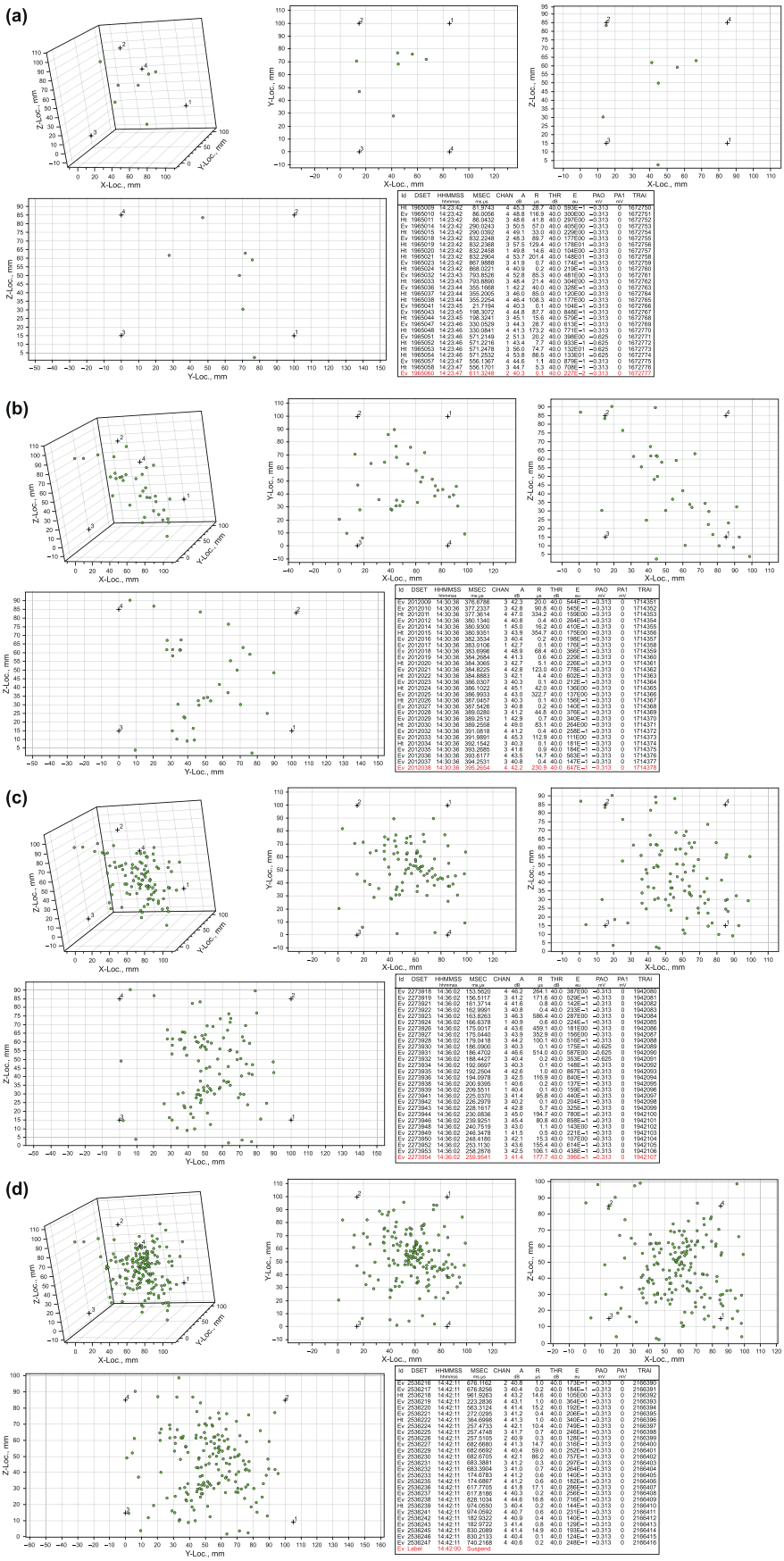

Fig. 16. The testing results of acoustic emission in Model I-2 in Fig. 8. **(a)** is the initial rupture stage; **(b)** and **(c)** show the intermediate rupture stage (0.5 and 0.75); **(d)** refers to the final rupture stage.

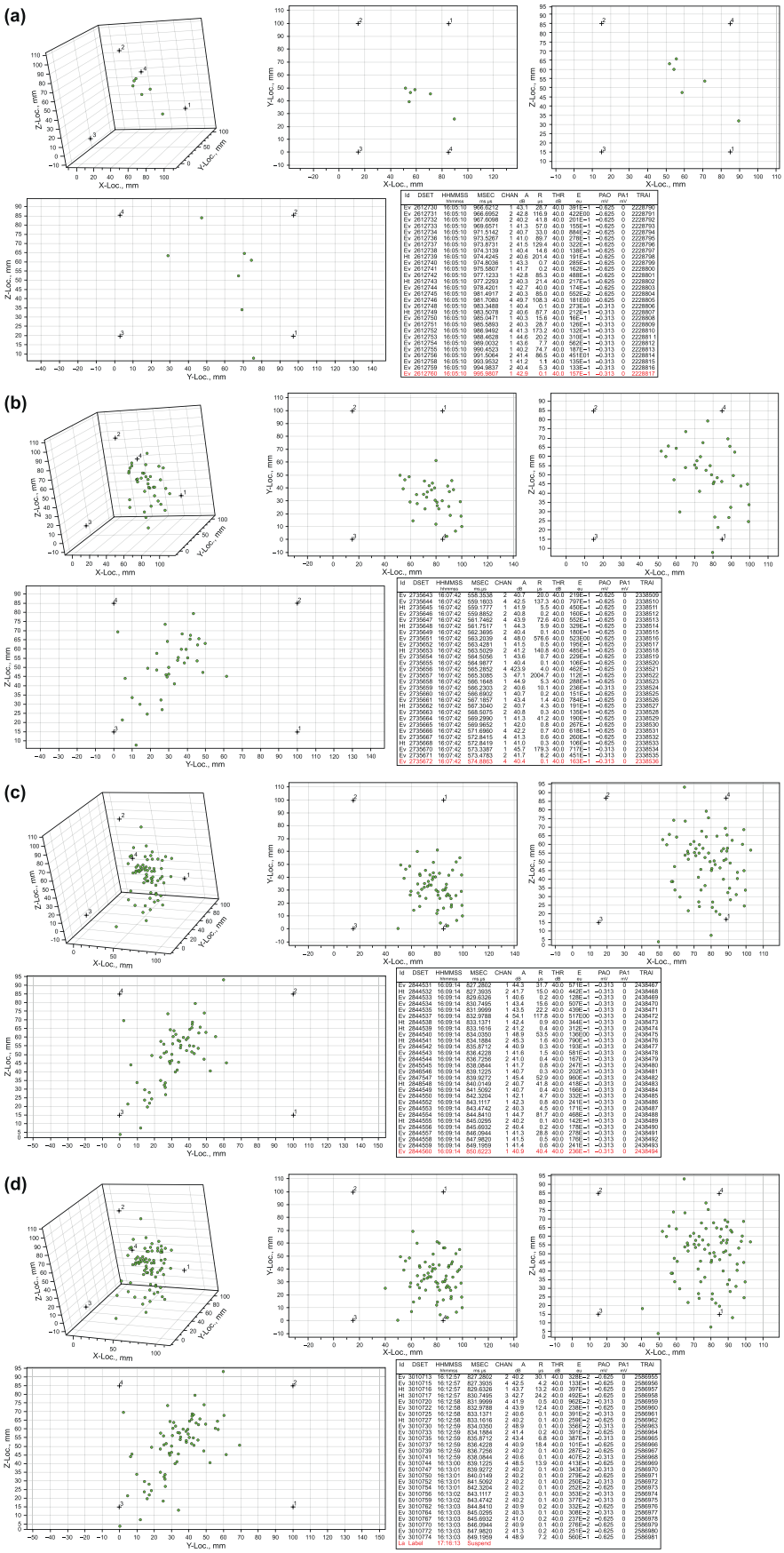

Fig. 17. The testing results of acoustic emission in Model I-3 in Fig. 8. **(a)** is the initial rupture stage; **(b)** and **(c)** show the intermediate rupture stage (0.5 and 0.75); **(d)** refers to the final rupture stage.

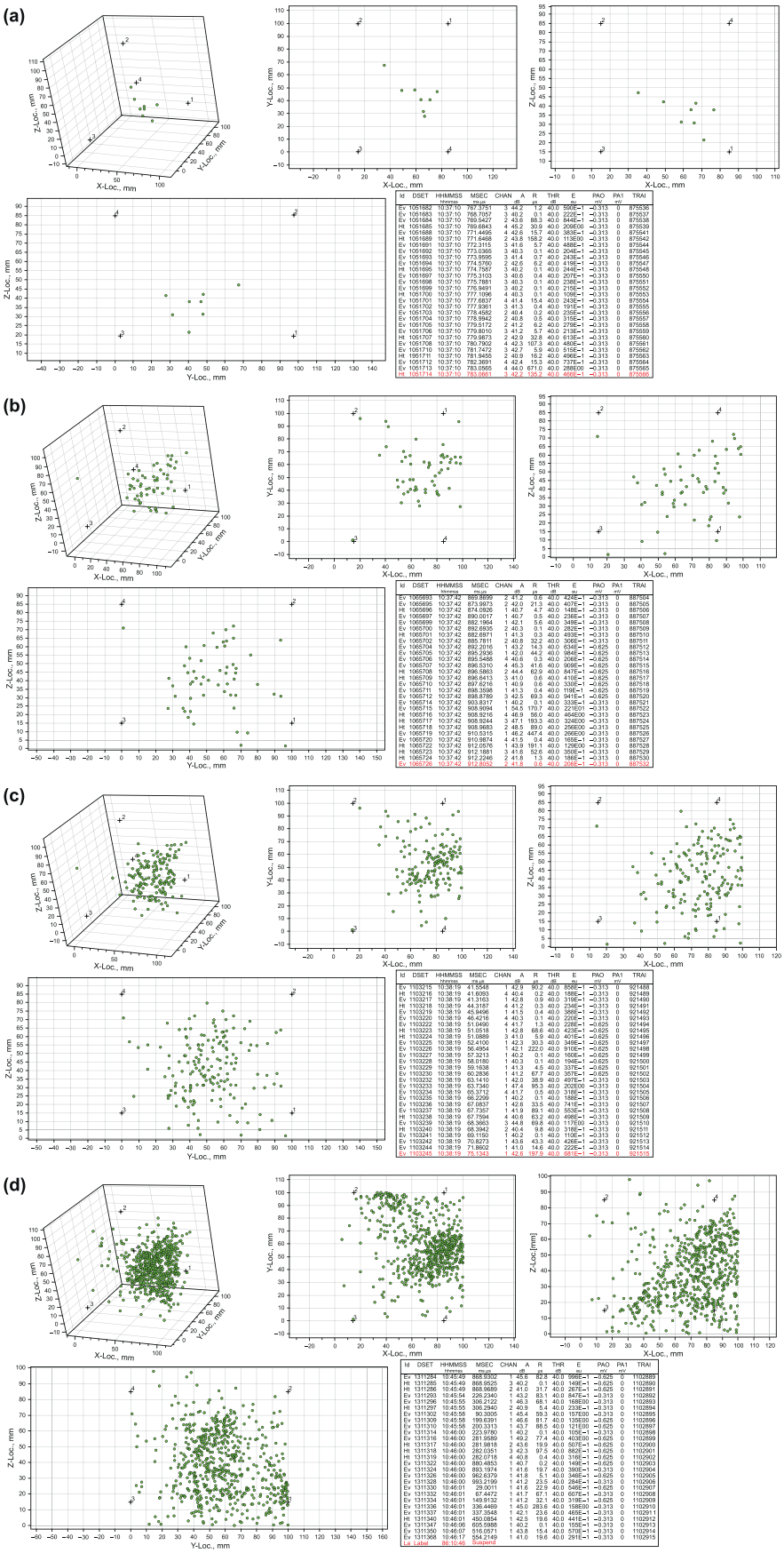

Fig. 18. The testing results of acoustic emission in Model II-2 in Fig. 8. **(a)** is the initial rupture stage; **(b)** and **(c)** show the intermediate rupture stage (0.5 and 0.75); **(d)** refers to the final rupture stage.

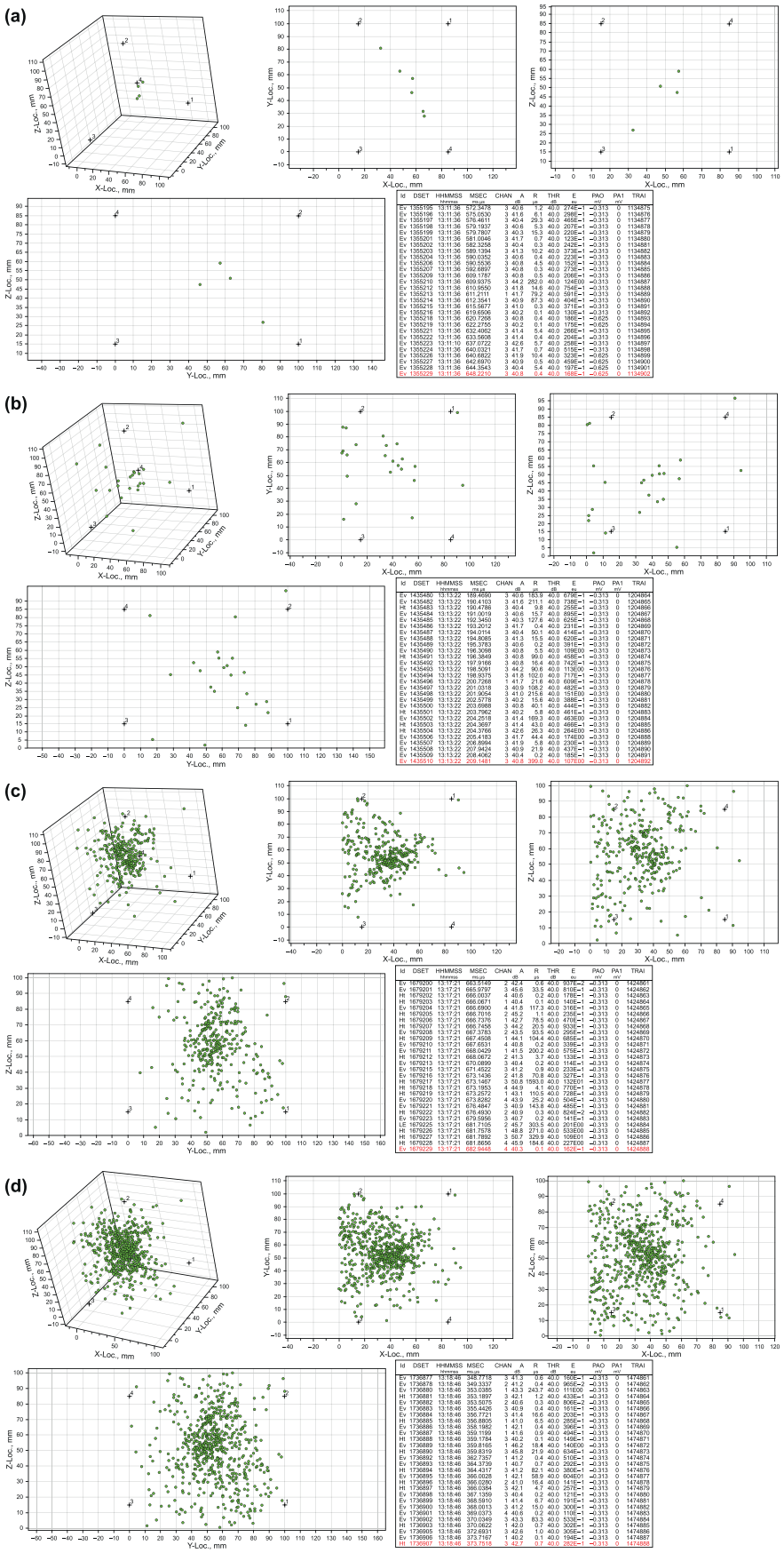

Fig. 19. The testing results of acoustic emission in Model III-1 in Fig. 8. **(a)** is the initial rupture stage; **(b)** and **(c)** show the intermediate rupture stage (0.5 and 0.75); **(d)** refers to the final rupture stage.

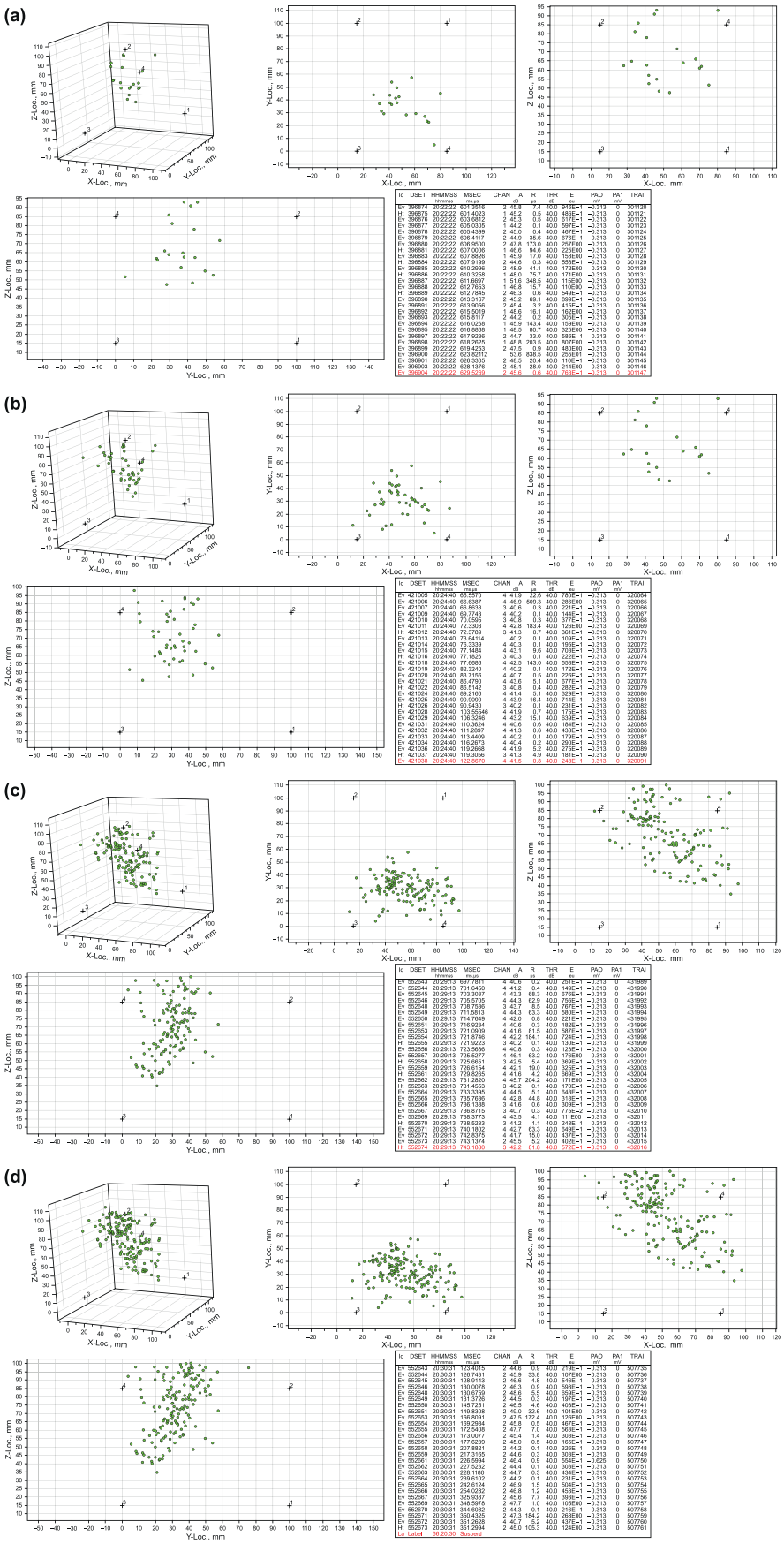

Fig. 20. The testing results of acoustic emission in Model III-2 in Fig. 8. **(a)** is the initial rupture stage; **(b)** and **(c)** show the intermediate rupture stage (0.5 and 0.75); **(d)** refers to the final rupture stage.

the formation of a conjugate fracture system (Fig. 16c). Notably, earlier formed fracturing fractures indicated long extension distances, while later fracturing fractures (restricted by the earlier ones) showed relatively smaller extension lengths. Consequently, a complex fracturing fracture system was formed, demonstrating good rupture capacity throughout the layer and extensive extension distance (Fig. 16d). Significantly, with an increase in confining pressure, later-formed fracturing fractures were further extended, with some penetrating the earlier ones. Additionally, constrained by the single cluster perforation throughout the layer, the fracturing fracture initially developed in the central area of the rock, revealing the largest rupture capacity in the middle layer (Fig. 17a). Gradually, a medium-high angle fracturing fracture was generated along the NE-SW (30°–50°) direction in the *Y-Z* plane, indicative of single group fractures (Fig. 17b). As the rupture area enlarged, the fracturing fracture extended further (Fig. 17c). Consequently, the fracturing fracture primarily distributed in the right lower quadrant of the rock, revealing the development of single group fracturing fractures (Fig. 17d). Overall, the fracturing fracture system was more developed in rocks with double cluster perforations compared to those with single cluster perforation.

Additionally, constrained by the double cluster perforations in Model II-2 (Fig. 8), the fracturing fracture initially ruptured in the medium and lower layers of the rock (Fig. 18a). The predominant direction of fracturing fracture was along the NE-SW (50°–70°) direction in the *Y-Z* plane. Subsequently, the fracturing fracture extended longer, and the rupture area enlarged (Fig. 18b). The rupture points along the predominant direction increased, and the fracturing fracture extended throughout the entire layer. Sequential development of the fracturing rupture led to the formation of two conjugate shear fractures, resulting in a complex fracturing fracture system (Fig. 18c). Consequently, the fracturing rupture increased significantly, and the complex fracturing fracture system was formed, indicating high angle fracturing fractures along the maximum principal stress direction (Fig. 18d). Similarly, restricted by the triple cluster perforations in Model III-1 (two perforations in each layer), the fracturing rupture was initially generated in the middle layer of the rock, indicating a rupture direction of NW-SE (320°–340 °) in the *X*-Y plane (Fig. 19a). Gradually, the fracturing fracture extended throughout the entire layer, and the rupture points increased (Fig. 19b). The predominant direction of the fracturing fracture was mainly along the NW-SE (300°–340°) direction, with the rupture direction of NE-SW (40°–60°) initially formed. Subsequently, the fracturing rupture was sequentially developed, with the earlier fracturing fracture extending longer (Fig. 19c). The later-formed fracturing fracture was restricted by the earlier one. Consequently, the complex fracturing fracture system was generated, with the rupture points primarily distributed in the middle area of the rock (Fig. 19d). Some of the later-formed fracturing fractures penetrated the earlier fracturing fracture, indicating a strong compressive stress environment. Additionally, constrained by the triple cluster perforation in Model III-2 (four perforations in each layer), the fracturing fracture initially ruptured in the upper and medium layers, indicating a good capacity to generate fractures (Fig. 20a). Gradually, the fracturing rupture was sequentially developed, and conjugate shear fractures were initially formed (Fig. 20b). One of the fracturing fracture systems was primarily along the NW-SE (300°–340°) direction, and the other was mainly in the NE-SW (30°–60°) direction. Subsequently, the fracturing fracture extended longer, and a conjugate fracturing fracture system was initially developed (Fig. 20c). Consequently, the relatively complex fracturing fracture system was formed, with the rupture points primarily distributed in the upper layer (Fig. 20d). The testing results from the AE showed good agreement with the physical experiment and numerical simulation results.

Comprehensively, four significant types of fracturing fractures were distinguished during the physical experiment, labeled as types I, II, III, and IV. In type I (Model I-1 and I-2), characterized by good rock cementation and a single-layer cluster hole mode with low angle or double layers with a middle angle, viscosity and displacement were 39.00 mPa s and 0.27 mL/s, respectively. Integrating AE testing results and visual observations from the physical experiments revealed an initial rupture direction along the minimum principal stress, with an arc turn towards the direction of the maximum principal stress. The maximum extension length and aperture of fracturing fractures were 40–50 mm and 0.50 mm, respectively. Additionally, the fractures exhibited a medium-high angle, indicating the ability to penetrate layers. Type II fractures, also exhibiting good rock cementation, featured a whole layer cluster hole model with a high angle (Model I-3 and Model IV). Viscosity and displacement were set at 39.00 mPa s and 0.27 mL/s, respectively. The initial rupture direction and extension were both along the maximum principal stress. The maximum extension length and aperture of fracturing fractures were 50 mm and 0.50–2.00 mm, respectively. These fractures displayed linear morphology and a medium-high angle, indicative of layer penetration characteristics. Type III fractures, characterized by poor rock cementation and a double layer or whole layer cluster hole model with a high angle (Model II-2 and Model III-1), had viscosity and displacement set at 228.00 mPa s and 1.33 mL/s, respectively. Fracturing fractures showed multidirectional initiation and extension, forming a more complex fracture system. The maximum extension length could reach 65.00–70.00 mm, with fracture apertures ranging from 0.50–1.00 mm, indicating superior fracturing performance. Similarly, type IV fractures, also featuring poor rock cementation and a double layer or whole layer cluster hole model with a high angle (Model II-1, II-3, and Model III-2), had viscosity and displacement set at 228.00 mPa s and 1.33 ml/s, respectively. The initial fracturing direction was along the maximum principal stress, with fractures extending obliquely along a small angle with the maximum principal stress. The maximum extension length and aperture of fracturing fractures were 50.00–65.00 mm and 0.40–0.70 mm, respectively. These fractures were characterized by intersection, arc, and radial morphology, exhibiting high or medium angles.

In conclusion, the extension direction and length of fracturing fractures were primarily controlled by the direction of maximum principal compressive stress. Initially, fracturing fractures ruptured at the minimum horizontal principal stress. If the stress intensity within the fracture surpassed the minimum horizontal principal stress in the adjacent formation, the fracture could penetrate the layer; otherwise, it was restricted by the layer. Poor cementation and compactness led to complex fracture morphology and the generation of network fractures. Strata with high elastic modulus increased the penetration ability of fracturing fractures, resulting in narrow and elongated features along the extension direction. Small Poisson's Ratio led to relatively larger fracture widths. Moreover, the interlayer development of fracturing fractures was influenced by strata occurrence. Fracture extension and development in vertical strata indicated dislocation. Fracture density varied according to the type of cluster perforation. Single-layer, low-angle, and double-helical cluster perforations all indicated high fracture density. Increased fracturing fluid displacement enlarged fracture length and height, while fracture width increased continuously before eventually leveling off. Low-cemented horizons and high-displacement, high-viscosity fracturing fluids were prone to generate more complex and extensively extended fractures.

6. Conclusions

In order to analyze the evolution mechanism of the fracturing fracture system, hydraulic fracturing physical experiments and finite element numerical simulations were conducted. Concurrently, rock mechanical testing, logging calculations, and seismic inversion technology were employed to obtain current in-situ stress and rock mechanical parameters, such as Young's Modulus and Poisson's Ratio. Additionally, Acoustic Emission (AE) testing and Finite Element Numerical Simulation (FENS) were applied to determine the internal characteristics of the fracturing fracture system.

(1) The Young's modulus in the study area ranged between 12.00 and 50.00 GPa, while Poisson's ratio was distributed between 0.15 and 0.24. The horizontal maximum and minimum principal stresses were concentrated in the ranges of 17.00–60.00 MPa and 11.00–40.00 MPa, respectively. Vertical principal stress ranged from 20.00 to 50.00 MPa, exhibiting a good correlation with depth. Where stress intensity was less than 5.00 MPa, effective fracturing occurred, easily generating meshed fractures.
(2) Increasing the distance from the cluster hole, the magnitude of the minimum principal stress initially increased and then decreased. A similar variation tendency was identified among stress intensity, equivalent elastic strain, and equivalent (von-Mises) stress, indicating three predominant directions to generate fracturing fractures. The largest values were identified along the cluster perforations, indicating the capacity to generate fracturing fractures.
(3) The extension direction and length of fracturing fractures were significantly influenced by the direction of the maximum horizontal principal stress. Increased fracturing fluid displacement enlarged fracture length and height, with fracture width continuously increasing before eventually leveling off. Low-cemented horizons, high-displacement, and high-viscosity fracturing fluids were prone to generating more complex and long extended fractures. This research provides theoretical support and effective guidance for hydraulic fracturing design in tight oil and gas reservoirs.

CRediT authorship contribution statement

Qi-Qiang Ren: Writing – review & editing, Writing – original draft, Software, Methodology, Conceptualization. **Li-Fei Li:** Data curation, Investigation. **Jin Wang:** Investigation. **Rong-Tao Jiang:** Formal analysis. **Meng-Ping Li:** Software, Data curation. **Jian-Wei Feng:** Supervision, Funding acquisition.

Declaration of competing interest

The authors declare that they have no known competing financial interests or personal relationships that could have appeared to influence the work reported in this paper.

Acknowledgement

This research was supported by the Major Scientific and Technological Projects of CNPC under grant ZD2019-183-006, the National Science and Technology Major Project of China (2016ZX05014002-006), and the National Natural Science Foundation of China (42072234). The authors would like to appreciate all the people, who supported the data, testing, and analyses. Many thanks to the anonymous reviewers, whose comments improve the quality of our manuscript.

References

Aimene, Y., Hammerquist, C., Ouenes, A., 2019. Anisotropic damage mechanics for asymmetric hydraulic fracture height propagation in a layered unconventional gas reservoir. J. Nat. Gas Sci. Eng. 67, 1–13. https://doi.org/10.1016/j.jngse.2019.04.013.

Andhumoudine, A.B., Nie, X., Zhou, Q.B., Yu, J., Kane, Q.I., Jin, L.D., Djaroun, R.R., 2021. Investigation of coal elastic properties based on digital core technology and finite element method. Adv. Geo. Energy Res. 5 (1), 53–63. https://doi.org/10.46690/ager.2021.01.06.

Bhattacharya, S., Nikolaou, M., 2016. Comprehensive optimization methodology for stimulation design of low-permeability unconventional gas reservoirs. SPE J. 21 (3), 947–964.. https://doi.org/10.2118/147622-PA.

Bostrom, N., Chertov, M., Pagels, M., Willberg, D., Chertova, A., Davis, M., Zagorski, W., 2014. The time-dependent permeability damage caused by fracture fluid. In: SPE International Symposium and Exhibition on Formation Damage Control. https://doi.org/10.2118/168140-MS. D011S006R001.

Cao, H., Zhu, H.L., Gao, Q., Chen, Y., Zhao, Y., Sun, P.H., 2022. Experimental investigation of the flow conductivity characteristics in shale's single fracture under the PHF stimulation. J. Petrol. Sci. Eng. 212, 110284. https://doi.org/10.1016/j.petrol.2022.110284.

Chang, X., Guo, Y.T., Zhou, J., Song, X.H., Yang, C.H., 2018. Numerical and experimental investigations of the interactions between hydraulic and natural fractures in shale formations. Energies 11 (10), 2541. https://doi.org/10.3390/en11102541.

Chang, X., Xu, E.S., Guo, Y.T., Yang, C.H., Hu, Z.W., Guo, W.H., 2022. Experimental study of hydraulic fracture initiation and propagation in deep shale with different injection methods. J. Petrol. Sci. Eng. 216, 110834. https://doi.org/10.1016/j.petrol.2022.110834.

Chen, J.L., Cai, X.Y., Lin, C.H., Wang, H.Y., Lei, M.S., 1999. Tectonic characteristics and episodic evolution of the northern fault depression in Songliao Basin. Acta Pet. Sin. 20, 14–18. https://doi.org/10.7623/syxb199904003.

Chen, W., Li, P., Peng, C.W., Zhang, B.R., 2010. Characteristics and controlling factors of pore features in the Putaohua oil reservoir in the Block Zhao-35, Daqing oilfield. Oil Gas Geol. 31 (6), 802–809. https://doi.org/10.11743/ogg20100613.

Chen, X., Li, Z.Q., Chen, J.L., Li, H.K., Zhang, T., 2010. Determination of the reverse period of Songliao Basin, China. Geol. Bull. China 29 (203), 305–311. https://doi.org/10.3969/j.issn.1671-2552.2010.02.015.

Chen, Y.J., Yin, T.B., Li, X.B., Li, Q., Yang, Z., Li, M.J., Wu, Y., 2021. Experimental investigation on dynamic mechanical behavior and fracture evolution of fissure-filled red sandstone after thermal treatment. Eng. Geol. 295, 106433. https://doi.org/10.1016/j.enggeo.2021.106433.

Chen, J.Z., Li, X.B., Cao, H., Zhu, Q.Q., 2022. Experimental study on the mechanism of coupled dynamic–static fracturing on damage evolution and crack propagation in tight shale. Energy Rep. 8, 7037–7062. https://doi.org/10.1016/j.egyr.2022.05.126.

Dehghanpour, H., Zubair, H.A., Chhabra, A., Ullah, A., 2012. Liquid intake of organic shales. Energy Fuels 26 (9), 5750–5758. https://doi.org/10.1021/ef3009794.

Diaz, M.B., Kim, K.Y., Jung, S.G., 2020. Effect of frequency during cyclic hydraulic fracturing and the process of the fracture development in laboratory experiments. Int. J. Rock Mech. Min. Sci. 134, 104474. https://doi.org/10.1016/j.ijrmms.2020.104474.

Fatah, A., Mahmud, H.B., Bennour, Z., Hossain, M., Gholami, R., 2021. Effect of supercritical CO_2 treatment on physical properties and functional groups of shales. Fuel 303, 121310. https://doi.org/10.1016/j.fuel.2021.121310.

Feng, Z.Q., Jia, C.Z., Xie, X.N., Zhang, S., Feng, Z.H., Timothy, A.C., 2010. Tectonostratigraphic units and stratigraphic sequences of the nonmarine Songliao basin, northeast China. Basin Res. 22 (1), 79–95. https://doi.org/10.1111/j.1365-2117.2009.00445.x.

Feng, Z.J., Zhang, S., Fu, X.L., 2012. Depositional evolution and accumulation response of Yaojia- Nenjiang Formation in Songliao Basin. Earth Sci. Front. 19 (1), 78.

Freeman, C.M., Moridis, G.J., Blasingame, T.A., 2011. A numerical study of microscale flow behavior in tight gas and shale gas reservoir systems. Transport Porous Media 90 (1), 253–268. https://doi.org/10.1007/s11242-011-9761-6.

Fu, X.F., Song, Y., 2008. Nontectonic mechanism of polygonal "T11" faults in the Sanzhao sag of Songliao basin. Acta Geol. Sin. 82 (6), 738–749. https://doi.org/10.3321/j.issn:0001-5717.2008.06.003.

Fu, X.F., Su, X.C., Gong, L., Wang, Q.Q., Gao, S., Xie, Z.H., 2023. Control of faults and fractures on shale oil enrichment. Geoenergy Science and Engineering 228, 212080. https://doi.org/10.1016/j.geoen.2023.212080.

Gale, J.F.W., Laubach, S.E., Olson, J.E., Eichhubl, P., Fall, A., 2014. Natural fractures in shale: a review and new observations natural fractures in shale: a review and new observations. AAPG Bull. 98 (11), 2165–2216. https://doi.org/10.1306/08121413151.

Gong, L., Liu, K.Q., Ju, W., 2023. Advances in the study of natural fractures in deep and unconventional reservoirs. Front. Earth Sc-Switz 10, 1096643. https://doi.org/10.3389/feart.2022.1096643.

He, J.C., Zhang, K.S., Liu, H.B., Tang, M.R., Zheng, X.L., Zhang, G.Q., 2022. Laboratory investigation on hydraulic fracture propagation in sandstone-mudstone-shale layers. Petrol. Sci. 19 (4), 1664–1673. https://doi.org/10.1016/j.petsci.2022.03.018.

Hooker, J.N., Cartwright, J., Stephenson, B., Silver, C.R.P., Dickson, A.J., Hsieh, Y.T., 2017. Fluid evolution in fracturing black shales, Appalachian Basin. AAPG (Am. Assoc. Pet. Geol.) Bull. 101 (8), 1203–1238. https://doi.org/10.1306/10031616030.

Hou, B., Chang, Z., Fu, W.N., Muhadasi, Y., Chen, M., 2019. Fracture initiation and propagation in a deep shale gas reservoir subject to an alternating-fluid-injection hydraulic-fracturing treatment. SPE J. 24 (4), 1839–1855. https://doi.org/10.2118/195571-PA.

Hu, Y., Gan, Q., Hurst, A., Elsworth, D., 2022. Hydraulic fracture propagation and interaction with natural fractures by coupled hydro-mechanical modeling. Geomech. Geophys. Geo. 8 (1), 1–26. https://doi.org/10.1007/s40948-021-00334-6.

Huang, L., Tong, H.M., Yang, D.H., Fan, J.Y., Huang, H.T., 2019. A new model for the formation and evolution of middle-shallow faults in the Daqing placanticline, Songliao Basin. Acta Geol. Sin. 93 (3), 597–605. https://doi.org/10.19762/j.cnki.dizhixuebao.2019040.

Huang, C.H., Zhu, H.Y., Wang, J.D., Han, J., Zhou, G.Q., Tang, X.H., 2022. A FEM-DFN model for the interaction and propagation of multi-cluster fractures during variable fluid-viscosity injection in layered shale oil reservoir. Petrol. Sci. 19 (6), 2796–2809. https://doi.org/10.1016/j.petsci.2022.06.007.

Huang, L.K., He, R., Yang, Z.Z., Tan, P., Chen, W.H., Li, X.G., Cao, A.W., 2023. Exploring hydraulic fracture behavior in glutenite formation with strong heterogeneity and variable lithology based on DEM simulation. Eng. Fract. Mech. 278, 109020. https://doi.org/10.1016/j.engfracmech.2022.109020.

Hunt, L., Reynolds, S., Hadley, S., Downton, J., Chopra, S., 2011. Causal fracture prediction: curvature, stress, and geomechanics. Lead. Edge. 30 (11), 1274–1286. https://doi.org/10.1190/1.3663400.

Islam, M.R., Hayashi, D., Kamruzzaman, A.B.M., 2009. Finite element modeling of stress distributions and problems for multi-slice longwall mining in Bangladesh, with special reference to the Barapukuria coal mine. Int. J. Coal Geol. 78 (2), 91–109. https://doi.org/10.1016/j.coal.2008.10.006.

Ju, Y., Wang, Y.L., Xu, B., Chen, J.L., Yang, Y.Q., 2019. Numerical analysis of the effects of bedded interfaces on hydraulic fracture propagation in tight multilayered reservoirs considering hydro-mechanical coupling. J. Petrol. Sci. Eng. 178, 356–375. https://doi.org/10.1016/j.petrol.2019.03.049.

Kim, J., Um, E.S., Moridis, G.J., 2018. Integrated simulation of vertical fracture propagation induced by water injection and its borehole electromagnetic responses in shale gas systems. J. Petrol. Sci. Eng. 165, 13–27. https://doi.org/10.1016/j.petrol.2018.01.024.

Laubach, S.E., 2003. Practical approaches to identifying sealed and open fractures. AAPG Bull. 87 (4), 561–579. https://doi.org/10.1306/11060201106.

Laubach, S.E., Diaz-Tushman, K., 2009. Laurentian palaeostress trajectories and ephemeral fracture permeability, cambrian eriboll formation sandstones west of the moine thrust zone, NW scotland. J. Geol. Soc. London 166 (2), 349–362. https://doi.org/10.1144/0016-76492008-061.

Li, H., Zou, Y.S., Valko, P.P., Ehlig-Economides, C., 2016. Hydraulic fracture height predictions in laminated shale formations using finite element discrete element method. In: SPE Hydraulic Fracturing Technology Conference. OnePetro. https://doi.org/10.2118/179129-MS.

Li, Z.H., Zhao, Q.Q., Teng, Y.T., Fan, M., Ripepi, N., Yin, X.L., Chen, C., 2022. Experimental investigation of non-monotonic fracture conductivity evolution in energy georeservoirs. J. Petrol. Sci. Eng. 211, 110103. https://doi.org/10.1016/j.petrol.2022.110103.

Lin, J.Y., Zhang, G., Yang, Q.J., Hao, A.H., 2003. Analysis on exploration potential of Fuyang reservoir in Daqing placanticline. Pet. Geol. Oilfield Dev. Daqing. 22, 16–18.

Lin, C., He, J.M., Li, X., Wan, X.L., Zheng, B., 2017. An experimental investigation into the effects of the anisotropy of shale on hydraulic fracture propagation. Rock Mech. Rock Eng. 50, 543–554. https://doi.org/10.1007/s00603-016-1136-4.

Liu, J.S., Ding, W.L., Wang, R.Y., Yin, S., Yang, H.M., Gu, Y., 2017. Simulation of paleotectonic stress fields and quantitative prediction of multi-period fractures in shale reservoirs: a case study of the Niutitang Formation in the Lower Cambrian in the Cen'gong block. South China. Mar. Petrol. Geol. 84, 289–310. https://doi.org/10.1016/j.marpetgeo.2017.04.004.

Lorenz, J.C., Hill, R.E., 1994. Subsurface fracture spacing: comparison of inferences from slant/horizontal and vertical cores. SPE Form. Eval. 9 (1), 66–72. https://doi.org/10.2118/21877-PA.

Lu, C., Li, M., Guo, J.C., Tang, X.H., Zhu, H.Y., Wang, Y.H., Liang, H., 2015. Engineering geological characteristics and the hydraulic fracture propagation mechanism of the sand-shale interbedded formation in the Xu5 reservoir. J. Geophys. Eng. 12 (3), 321–339. https://doi.org/10.1088/1742-2132/12/3/321.

Luo, A., Li, Y.M., Wu, L., Peng, Y., Tang, W., 2021. Fractured horizontal well productivity model for shale gas considering stress sensitivity, hydraulic fracture azimuth, and interference between fractures. Natural Gas Industry B 8 (3), 278–286. https://doi.org/10.1016/j.ngib.2021.04.008.

Lyu, Q., Tan, J.Q., Dick, J.M., Liu, Q., Gamage, R.P., Wang, Z.H., Hu, C.G., 2019. Stress–strain modeling and brittleness variations of low-clay shales with CO_2/CO_2-water imbibition. Rock Mech. Rock Eng. 52 (7), 2039–2052. https://doi.org/10.1007/s00603-018-1687-7.

Mathews, J.P., Campbell, Q.P., Xu, H., Halleck, P., 2017. A review of the application of X-ray computed tomography to the study of coal. Fuel 209, 10–24. https://doi.org/10.1016/j.fuel.2017.07.079.

Miehe, C., Hofacker, M., Schänzel, L.M., Aldakheel, F., 2015. Phase field modeling of fracture in multi-physics problems. Part II. Coupled brittle-to-ductile failure criteria and crack propagation in thermo-elastic–plastic solids. Cmame 294, 486–522. https://doi.org/10.1016/j.cma.2014.11.017.

Mohammadnejad, T., Andrade, J.E., 2016. Numerical modeling of hydraulic fracture propagation, closure and reopening using XFEM with application to in-situ stress estimation. Int. J. Numer. Anal. Model. 40 (15), 2033–2060. https://doi.org/10.1002/nag.2512.

Morley, C.K., Hagke, C.V., Hansberry, R.L., Collins, A.S., Kanitpanyacharoen, W., King, R., 2017. Review of major shale-dominated detachment and thrust characteristics in the diagenetic zone: Part I, meso-and macro-scopic scale. Earth Sci. Rev. 173, 168–228. https://doi.org/10.1016/j.earscirev.2017.07.019.

Morley, C.K., Hagke, C.V., Hansberry, R., Collins, A., Kanitpanyacharoen, W., King, R., 2018. Review of major shale-dominated detachment and thrust characteristics in the diagenetic zone: Part II, rock mechanics and microscopic scale. Earth Sci. Rev. 176, 19–50. https://doi.org/10.1016/j.earscirev.2017.09.015.

Nguyen-Le, V., Shin, H., 2022. Artificial neural network prediction models for Montney shale gas production profile based on reservoir and fracture network parameters. Energy 244, 123150. https://doi.org/10.1016/j.energy.2022.123150.

Niu, C.Y., Zhu, Z.M., Zhou, L., Li, X.H., Ying, P., Dong, Y.Q., Deng, S., 2021. Study on the microscopic damage evolution and dynamic fracture properties of sandstone under freeze-thaw cycles. Cold Reg. Sci. Technol. 191, 103328. https://doi.org/10.1016/j.coldregions.2021.103328.

Pope, C.D., Palisch, T., Saldungaray, P., 2012. Improving completion and stimulation effectiveness in unconventional reservoirs-field results in the eagle ford shale of north America. In: SPE/EAGE European Unconventional Resources Conference and Exhibition-form Potential to Production. https://doi.org/10.2118/152839-MS.

Rabczuk, T., Gracie, R., Song, J.H., Belytschko, T., 2010. Immersed particle method for fluid–structure interaction. Int. J. Numer. Methods Eng. 81 (1), 48–71. https://doi.org/10.1002/nme.2670.

Ranjith, P.G., Wanniarachchi, W.A.M., Perera, M.S.A., Rathnaweera, T.D., 2018. Investigation of the effect of foam flow rate on foam-based hydraulic fracturing of shale reservoir rocks with natural fractures: an experimental study. J. Petrol. Sci. Eng. 169, 518–531. https://doi.org/10.1016/j.petrol.2018.06.002.

Rege, K., Lemu, H.G., 2017. A review of fatigue crack propagation modelling techniques using FEM and XFEM. In: IOP Conference Series: Materials Science and Engineering, vol. 276. IOP Publishing, 012027. https://doi.org/10.1088/1757-899X/276/1/012027.

Ren, Q.Q., Jin, Q., Feng, J.W., Li, M.P., 2019. Simulation of stress fields and quantitative prediction of fractures distribution in upper Ordovician biological limestone formation within Hetianhe field, Tarim Basin, NW China. J. Petrol. Sci. Eng. 173, 1236–1253. https://doi.org/10.1016/j.petrol.2018.10.081.

Ren, Q.Q., Jin, Q., Feng, J.W., Li, Z.Y., Du, H., 2020. Geomechanical models for the quantitatively prediction of multi-scale fracture distribution in carbonate reservoirs. J. Struct. Geol. 135, 104033. https://doi.org/10.1016/j.jsg.2020.104033.

Ren, Q.Q., Feng, J.W., Johnston, S., Zhao, L.B., 2021. The influence of argillaceous content in carbonate rocks on the 3D modeling and characterization of tectonic fracture parameters—example from the carboniferous and ordovician formations in the hetianhe gas field, Tarim Basin, NW China. J. Petrol. Sci. Eng. 203, 108668. https://doi.org/10.1016/j.petrol.2021.108668.

Ren, L., Yu, Z.H., Zhao, J.Z., Lin, R., Wu, J.F., Wu, J.J., Song, Y., 2022. Hydraulic fractures simulation in non-uniform stress field of horizontal shale gas well. J. Petrol. Sci. Eng. 216, 110843. https://doi.org/10.1016/j.petrol.2022.110843.

Si, S.H., Hu, Z.M., Liu, J., Liu, Y.F., Er, C., Yang, Z.H., He, J.H., 2021. Relationship between reservoir densification and hydrocarbon charging: a case study of cretaceous Fuyu reservoir of the Sanzhao sag. Geoscience 35 (6), 1854. https://doi.org/10.19657/j.geoscience.1000-8527.2021.195.

Stumpf, H., Makowski, J., Hackl, K., 2009. Dynamical evolution of fracture process region in ductile materials. Int. J. Plast. 25 (5), 995–1010. https://doi.org/10.1016/j.ijplas.2008.04.004.

Su, A., Chen, H.H., Feng, Y.X., Zhao, J.X., Nquyen, A.D., 2022. Multistage fracturing history in the Paleocene lacustrine shale oil reservoirs of the Subei Basin, Eastern China. Mar. Petrol. Geol. 144, 105835. https://doi.org/10.1016/j.marpetgeo.2022.105835.

Sun, Y., Yu, L.M., Yan, B.Q., Liu, Y.Y., Cong, L., Ma, S.Z., 2018. Oil-water distribution and its major controlling factors of Putaohua reservoirs of the cretaceous Yaojia Formation in syncline area of Sanzhao sag, Songliao Basin. Oil Gas Geol. 39 (6), 1120–1130. https://doi.org/10.11743/ogg20180603.

Tan, J.Q., Hu, C.E., Lyu, Q., F, G., Chen, S.F., 2022. Experimental investigation on the effects of different fracturing fluids on shale surface morphology. J. Petrol. Sci. Eng. 212, 110356. https://doi.org/10.1016/j.petrol.2022.110356.

Tan, P., Chen, Z.W., Fu, S.H., Zhao, Q., 2023. Experimental investigation on fracture growth for integrated hydraulic fracturing in multiple gas bearing formations. Geoenergy Science and Engineering 231, 212316. https://doi.org/10.1016/j.geoen.2023.212316.

Vermylen, J.P., Zoback, M.D., 2011. Hydraulic fracturing, microseismic magnitudes, and stress evolution in the Barnett Shale, Texas, USA. In: SPE Hydraulic Fracturing Technology Conference. OnePetro. https://doi.org/10.2118/140507-MS.

Wang, K., Dai, J.S., Feng, J.W., Wang, J.P., Li, Q., 2014. Research on reservoir rock mechanical parameters of Keshen foreland thrust belt in Tarim Basin. Journal of China University of Petroleum (Edition of Natural Science) 5, 25–33. https://doi.org/10.3969/j.issn.1673-5005.2014.05.004 (in Chinese).

Wang, H., Liu, H., Wu, H.A., Wang, X.X., 2015. A 3D numerical model for studying the effect of interface shear failure on hydraulic fracture height containment. J. Petrol. Sci. Eng. 133, 280–284. https://doi.org/10.1016/j.petrol.2015.06.016.

Wang, T.T., Ramezani, J., Wang, C.S., Wu, H.C., He, H.Y., Bowring, S.A., 2016. High-precision U–Pb geochronologic constraints on the Late Cretaceous terrestrial

cyclostratigraphy and geomagnetic polarity from the Songliao Basin, Northeast China. Earth Planet Sci. Lett. 446, 37–44. https://doi.org/10.1016/j.epsl.2016.04.007.
Wei, Y.S., Wang, J.L., Yu, W., Qi, Y.D., Miao, J.J., Yuan, H., Liu, C.X., 2021. A smart productivity evaluation method for shale gas wells based on 3D fractal fracture network model. Petrol. Explor. Dev. 48 (4), 911–922. https://doi.org/10.1016/S1876-3804(21)60076-9.
Weinberg, K., Wieners, C., 2022. Dynamic phase-field fracture with a first-order discontinuous galerkin method for elastic waves. Comput. Methods Appl. Math. 389, 114330. https://doi.org/10.1016/j.cma.2021.114330.
Wen, Q.Z., Wang, S.T., Duan, X.F., Li, Y., Wang, F., Jin, X.C., 2016. Experimental investigation of proppant settling in complex hydraulic-natural fracture system in shale reservoirs. J. Nat. Gas Sci. Eng. 33, 70–80. https://doi.org/10.1016/j.jngse.2016.05.010.
Westwood, R.F., Toon, S.M., Styles, P., Cassidy, N.J., 2017. Horizontal respect distance for hydraulic fracturing in the vicinity of existing faults in deep geological reservoirs: a review and modelling study. Geomech Geophys. Geo. 3 (4), 379–391. https://doi.org/10.1007/s40948-017-0065-3.
Wick, T., 2016. Coupling fluid–structure interaction with phase-field fracture. J. Comput. Phys. 327, 67–96. https://doi.org/10.1016/j.jcp.2016.09.024.
Williams, V., McCartney, E., Nino-Penaloza, A., 2016. Far-field diversion in hydraulic fracturing and acid fracturing: using solid particulates to improve stimulation efficiency. In: SPE Asia Pacific Hydraulic Fracturing Conference. OnePetro. https://doi.org/10.2118/181845-MS.
Wu, F.Y., Sun, D.Y., Li, H.M., Wang, X.L., 2001. The nature of basement beneath the Songliao Basin in NE China: geochemical and isotopic constraints. Phys. Chem. Earth Solid Earth Geodes. 26 (9–10), 793–803. https://doi.org/10.1016/S1464-1895(01)00128-4.
Wu, Y.S., Li, J.F., Ding, D.Y., Wang, C., Di, Y., 2014. A generalized framework model for the simulation of gas production in unconventional gas reservoirs. SPE J. 19 (5), 845–857. https://doi.org/10.2118/163609-PA.
Xia, Q., 2020. Oil-water distribution laws and main controlling factors of Putaohua reservoirs in Block Gu628 of Xinzhao Oilfield. Pet. Geol. Oilfield Dev. Daqing 39 (5), 25–33. https://doi.org/10.19597/J.ISSN.1000-3754.201912024.
Yang, K.G., Gao, D.L., 2022. Numerical simulation of hydraulic fracturing process with consideration of fluid–solid interaction in shale rock. J. Nat. Gas Sci. Eng. 102, 104580. https://doi.org/10.1016/j.jngse.2022.104580.
Zeng, Q.D., Liu, W.Z., Yao, J., 2018. Hydro-mechanical modeling of hydraulic fracture propagation based on embedded discrete fracture model and extended finite element method. J. Petrol. Sci. Eng. 167, 64–77. https://doi.org/10.1016/j.petrol.2018.03.086.
Zeng, L.B., Gong, L., Guan, C., Zhang, B.J., Wang, Q.Q., Zeng, Q., Lyu, W.Y., 2022. Natural fractures and their contribution to tight gas conglomerate reservoirs: a case study in the northwestern Sichuan Basin, China. J. Petrol. Sci. Eng. 210, 110028. https://doi.org/10.1016/j.petrol.2021.110028.
Zhang, Q., Zhang, X.P., Sun, W., 2021. A review of laboratory studies and theoretical analysis for the interaction mode between induced hydraulic fractures and pre-existing fractures. J. Nat. Gas Sci. Eng. 86, 103719. https://doi.org/10.1016/j.jngse.2020.103719.
Zhang, C., Liu, D.D., Jiang, Z.X., Song, Y., Luo, Q., Wang, X., 2022a. Mechanism for the formation of natural fractures and their effects on shale oil accumulation in Junggar Basin, NW China. Int. J. Coal Geol. 254, 103973. https://doi.org/10.1016/j.coal.2022.103973.
Zhang, T., Liu, B., Wei, Z., Jiao, Z.H., Song, Z.Y., Zhang, H.W., 2022b. Dynamic mechanical responses and crack evolution of burst-prone coal with a single prefabricated fissure. Theor. Appl. Fract. Mech. 121, 103494. https://doi.org/10.1016/j.tafmec.2022.103494.
Zhao, H., Liang, B., Sun, W.J., Hu, Z.M., Ma, Y.Q., Liu, Q., 2022a. Effects of hydrostatic pressure on hydraulic fracturing properties of shale using X-ray computed tomography and acoustic emission. J. Petrol. Sci. Eng. 110725. https://doi.org/10.1016/j.petrol.2022.110725.
Zhao, X.Z., Jin, F.M., Liu, X.W., Zhang, Z., Cong, Z.Y., Li, Z.J., Tang, J.Z., 2022b. Numerical study of fracture dynamics in different shale fabric facies by integrating machine learning and 3-D lattice method: a case from Cangdong Sag, Bohai Bay basin, China. J. Petrol. Sci. Eng. 110861. https://doi.org/10.1016/j.petrol.2022.110861.
Zhao, Z.H., Liu, Z.Q., Lu, C., He, T., Chen, M.L., 2022c. Brittleness evaluation based on shale fracture morphology. J. Nat. Gas Sci. Eng. 104, 104679. https://doi.org/10.1016/j.jngse.2022.104679.
Zheng, Y.X., He, R., Huang, L.K., Bai, Y.S., Wang, C., Chen, W.H., Wang, W., 2022. Exploring the effect of engineering parameters on the penetration of hydraulic fractures through bedding planes in different propagation regimes. Comput. Geotech. 146, 104736. https://doi.org/10.1016/j.compgeo.2022.104736.
Zhou, Z.L., Zhang, G.Q., Dong, H.R., Liu, Z.B., Nie, Y.X., 2017. Creating a network of hydraulic fractures by cyclic pumping. Int. J. Rock. Mech. Min. 97, 52–63. https://doi.org/10.1016/j.ijrmms.2017.06.009.
Zhou, T., Wang, H.B., Li, F.X., Li, Y.Z., Zhang, C., 2020. Numerical simulation of hydraulic fracture propagation in laminated shale reservoirs. Petrol. Explor. Dev. 47 (5), 1117–1130. https://doi.org/10.1016/S1876-3804(20)60122-7, 2020.
Zhou, Y., You, L.J., Kang, Y.L., Xie, B.B., Cheng, Q.Y., 2022. Experimental study of the fracture initiation through the synergy of spontaneous imbibition and hydration of residual fracturing fluids in shale gas reservoirs. J. Nat. Gas Sci. Eng. 102, 104577. https://doi.org/10.1016/j.jngse.2022.104577.
Zhu, H.Y., Tang, X.H., Song, Y.J., Li, K.D., Xiao, J.L., Dusseault, M.B., Mclennan, J.D., 2021. An infill well fracturing model and its micro seismic events barrier effect: a case in fuling shale gas reservoir. SPE J. 26 (1), 113–134. https://doi.org/10.2118/202485-PA.
Zoback, M.D., 2019. Unconventional Reservoir Geomechanics. Cambridge university press, Cambridge, UK. https://doi.org/10.1017/9781316091869.
Zou, Y.S., Ma, X.F., Zhou, T., Li, N., Chen, M., Li, S.H., Zhang, Y.N., Li, H., 2017. Hydraulic fracture growth in a layered formation based on fracturing experiments and discrete element modeling. Rock Mech. Rock Eng. 50 (9), 2381–2395. https://doi.org/10.1007/s00603-017-1241-z.